



NAVAL POSTGRADUATE SCHOOL

MONTEREY, CALIFORNIA

THESIS

LASER PULSE SHAPING FOR LOW EMITTANCE PHOTO-INJECTOR

by

Conor Michael Pogue

June 2012

Thesis Co-Advisors:

William Colson

Keith Cohn

Second Reader:

Joe Blau

Approved for public release; distribution is unlimited

THIS PAGE INTENTIONALLY LEFT BLANK

REPORT DOCUMENTATION PAGE			<i>Form Approved OMB No. 0704-0188</i>	
Public reporting burden for this collection of information is estimated to average 1 hour per response, including the time for reviewing instruction, searching existing data sources, gathering and maintaining the data needed, and completing and reviewing the collection of information. Send comments regarding this burden estimate or any other aspect of this collection of information, including suggestions for reducing this burden, to Washington headquarters Services, Directorate for Information Operations and Reports, 1215 Jefferson Davis Highway, Suite 1204, Arlington, VA 22202-4302, and to the Office of Management and Budget, Paperwork Reduction Project (0704-0188) Washington DC 20503.				
1. AGENCY USE ONLY (Leave blank)		2. REPORT DATE June 2012	3. REPORT TYPE AND DATES COVERED Master's Thesis	
4. TITLE AND SUBTITLE Laser Pulse Shaping for Low Emittance Photo-Injector			5. FUNDING NUMBERS	
6. AUTHOR(S) Conor Michael Pogue				
7. PERFORMING ORGANIZATION NAME(S) AND ADDRESS(ES) Naval Postgraduate School Monterey, CA 93943-5000			8. PERFORMING ORGANIZATION REPORT NUMBER	
9. SPONSORING /MONITORING AGENCY NAME(S) AND ADDRESS(ES) N/A			10. SPONSORING/MONITORING AGENCY REPORT NUMBER	
11. SUPPLEMENTARY NOTES The views expressed in this thesis are those of the author and do not reflect the official policy or position of the Department of Defense or the U.S. Government. IRB Protocol number _____N/A_____.				
12a. DISTRIBUTION / AVAILABILITY STATEMENT Approved for public release; distribution is unlimited			12b. DISTRIBUTION CODE A	
13. ABSTRACT (maximum 200 words) Fourth generation light sources are pushing the boundaries of high intensity, coherent, short wavelength light sources for the scientific community. In the step from the 3rd generation to the 4th, a Free Electron Laser (FEL) amplifier is used to generate the light over the synchrotron rings of the past. To get to the short wavelengths of an X-ray FEL the emittance of the electron beam must be tightly controlled to match the emittance of the short wavelength photons they are interacting with. The emittance is an intrinsic property of an electron beam and can only be harmed as it propagates through a beam line. Due to this, it is important to start with as low as emittance as possible. Minimizing the electron beam emittance has the added benefit of decreasing the gain length needed to get up to higher power. For this reason low emittance is important for all types of FEL schemes. Most injector schemes use a photo-cathode as the electron beam source. A way to keep the emittance low is to shape the laser beam that generates the electrons as it imparts energy into the photo-cathode. Research was done in shaping the drive laser using a set of birefringent crystals for the APEX project at Lawrence Berkeley National Lab. The thesis discusses the light sources as a whole, the physics behind the pulse shaping technique as well as results obtained.				
14. SUBJECT TERMS Free Electron Laser, Photoinjector Drive Laser, Laser Pulse Shaping			15. NUMBER OF PAGES 89	
			16. PRICE CODE	
17. SECURITY CLASSIFICATION OF REPORT Unclassified	18. SECURITY CLASSIFICATION OF THIS PAGE Unclassified	19. SECURITY CLASSIFICATION OF ABSTRACT Unclassified	20. LIMITATION OF ABSTRACT UU	

THIS PAGE INTENTIONALLY LEFT BLANK

Approved for public release; distribution is unlimited

LASER PULSE SHAPING FOR LOW EMITTANCE PHOTO-INJECTOR

Conor Michael Pogue
Civilian
B.S. University of California Santa Barbara, 2010

Submitted in partial fulfillment of the
requirements for the degree of

MASTER OF SCIENCE IN PHYSICS

from the

**NAVAL POSTGRADUATE SCHOOL
JUNE 2012**

Author: Conor Pogue

Approved by: William B. Colson
Thesis Co-Advisor

Keith Cohn
Thesis Co-Advisor

Joseph Blau
Second Reader

Andrés Larraza
Chair, Department of Physics

THIS PAGE INTENTIONALLY LEFT BLANK

ABSTRACT

Fourth generation light sources are pushing the boundaries of high intensity, coherent, short wavelength light sources for the scientific community. In the step from the 3rd generation to the 4th, a Free Electron Laser (FEL) amplifier is used to generate the light over the synchrotron rings of the past. To get to the short wavelengths of an X-ray FEL the emittance of the electron beam must be tightly controlled to match the emittance of the short wavelength photons they are interacting with. The emittance is an intrinsic property of an electron beam and can only be harmed as it propagates through a beam line. Due to this, it is important to start with as low as emittance as possible. Minimizing the electron beam emittance has the added benefit of decreasing the gain length needed to get up to higher power. For this reason low emittance is important for all types of FEL schemes. Most injector schemes use a photo-cathode as the electron beam source. A way to keep the emittance low is to shape the laser beam that generates the electrons as it imparts energy into the photo-cathode. Research was done in shaping the drive laser using a set of birefringent crystals for the APEX project at Lawrence Berkeley National Lab. The thesis discusses the light sources as a whole, the physics behind the pulse shaping technique as well as results obtained.

THIS PAGE INTENTIONALLY LEFT BLANK

TABLE OF CONTENTS

I.	INTRODUCTION.....	1
A.	EVOLUTION OF LIGHT SOURCES	1
B.	APPLICATIONS	3
II.	FOURTH GENERATION LIGHT SOURCES	5
A.	COMPONENTS.....	5
1.	Electron Beam Generation / Injector.....	5
a.	<i>Cathodes</i>	<i>6</i>
b.	<i>Accelerating Cavity</i>	<i>7</i>
2.	Linear Accelerators (LINACs)	8
3.	Undulator.....	9
4.	Beam Control	10
B.	FEL INTERACTION	10
1.	Resonance Condition	11
2.	Pendulum Phase Space	12
3.	FEL Pendulum Equation, Microscopic Electron Evolution	13
4.	FEL Wave Equation	15
III.	THE NEXT GENERATION LIGHT SOURCE (NGLS)	17
A.	BASIC DESIGN	18
B.	INJECTOR.....	18
IV.	ELECTRON BEAMM CREATION AND DYNAMICS	21
A.	ELECTRON BEAM CREATION / PHOTOELECTRIC EFFECT	21
1.	Bunch Charge.....	21
2.	Bunch Shape.....	22
3.	Emittance Matching.....	23
V.	OPTICAL PROPERTIES.....	25
A.	PROPERTIES OF LIGHT	25
1.	Polarization.....	25
2.	Wave Packet	25
B.	REFRACTIVE INDEX	26
1.	Dispersion	27
2.	Birefringence	29
VI.	APEX LASER PULSE SHAPING	31
A.	LASER PULSE LENGTH	31
B.	APEX DRIVE LASER	32
C.	LASER PULSE SHAPING TECHNIQUE.....	34
1.	Transverse Pulse Shaping	34
2.	Longitudinal Pulse Shaping	35
D.	PULSE STACKING CODE.....	38
E.	CALCULATIONS	39
VII.	EXPERIMENT	45

A.	INITIAL EXPERIMENTAL SETUP	45
1.	Measuring Laser Polarization	45
2.	Controlling Laser Polarization	46
3.	Initial Laser Polarization	46
4.	Initial Crystal Alignment	47
B.	UV POWER LOSS	48
C.	LONGITUDINAL PULSE SHAPE MEASUREMENT	48
1.	Sweep Unit	50
2.	Operating Regimes.....	51
D.	MEASUREMENT CAPABILITIES	52
E.	RESULTS	54
1.	No Crystal	54
2.	First Crystal.....	55
a.	<i>One Crystal Angle Study</i>	56
3.	Two Crystals.....	57
a.	<i>Two Crystal Angle Study</i>	58
4.	Three Crystals	60
5.	Six Crystals	61
F.	POSSIBLE SOURCES OF ERROR	63
1.	Systematic Errors.....	63
2.	Random Errors	64
VIII.	CONCLUSION	65
	LIST OF REFERENCES	67
	INITIAL DISTRIBUTION LIST	71

LIST OF FIGURES

Figure 1.	Schematic of 3 ½ cell RF photoinjector. From [10].	6
Figure 2.	Cross-Section of generic cavity showing longitudinal E-field and transverse B-field (TM01 mode). From [12].	8
Figure 3.	Schematic of linear undulator setup causing transverse electron oscillation. From [13].	9
Figure 4.	Schematic of “electron-photon” race. From [15].	11
Figure 5.	Phase space plot of simple pendulum. From [16].	13
Figure 6.	Shows a typical phase space plot for the FEL interaction. Each “+” represents the final phase space coordinate (ζ, v) of an electron.	15
Figure 7.	Schematic of NGLS proposed layout. After [24]	17
Figure 8.	Cross Section of APEX design. From [25].	19
Figure 9.	The ellipsoid vs. the cylindrical pulse shape	23
Figure 10.	Depiction of elliptical and circular polarization [33].	25
Figure 11.	Demonstrates the wave packet as being a superposition of waves with separate frequencies. After [34].	26
Figure 12.	Dispersion curve showing the refractive index of Fused Silica as a function of wavelength. From [35]	27
Figure 13.	Index ellipsoid for uniaxial crystal depicting the polarization dependent refractive indices. This shows the propagation direction S, the optical axis OA, the polarization of the o-wave (n_o), and the polarization of the e-wave (n_e). After [39].	29
Figure 14.	Illustration of accelerating gradient magnitude and short electron bunch length. From [25]	31
Figure 15.	Illustration of accelerating gradient magnitude and long electron bunch length. From [25]	32
Figure 16.	Schematic of APEX drive laser	34
Figure 17.	Illustrates summation of temporally spread Gaussians with alternating polarizations (denoted red and blue)	36
Figure 18.	Illustration of delay and polarization shift by a birefringent crystal	37
Figure 19.	Longitudinal profiles from simulation (0.6 ps initial pulse)	40
Figure 20.	Measured UV spectrum of laser pulse	41
Figure 21.	Longitudinal profiles from simulation (1.07 ps initial pulse)	43
Figure 22.	Diagram of polarizing beam splitter cube	45
Figure 23.	Diagram of key components of streak camera. From [51]	49
Figure 24.	Different types of sweep voltages from Streak Camera. After [51]	50
Figure 25.	The jitter caused by the varying arrival time of the incident laser pulse	51
Figure 26.	Streak image and profile analysis from Streak Camera	52
Figure 27.	Simulation of pulse profile of green light shaped by six crystal pulse stacker	54
Figure 28.	Initial laser pulse before any pulse forming	55
Figure 29.	Individual sub-pulses after 35 mm crystal	56

Figure 30.	The effect of varying the alignment angle ($\Delta\theta_1$) of a single crystal. The extraordinary pulse is on the left and the ordinary pulse on the right in each profile. (Horizontal axes: Time (ps), Vertical Axes: Intensity (AU))	57
Figure 31.	Pulse envelope after the 35 mm and 17.5 mm crystals.....	58
Figure 32.	Two crystal study. The first crystal is optimally aligned ($\Delta\theta_1=0$), and the second crystal's alignment angle is varied from its nominal value ($\theta_2=45^\circ$) by $\Delta\theta_2 = \pm 5^\circ$ and $\pm 10^\circ$ (Horizontal axes Time (ps), Vertical Axes Intensity (AU)).....	59
Figure 33.	Two crystal study. Both crystals are initially optimally aligned ($\Delta\theta_1 = \Delta\theta_2 = 0$). The first crystal is then misaligned by $\Delta\theta_1 = \pm 5^\circ$ and $\pm 10^\circ$ (Horizontal axes Time (ps), Vertical Axes Intensity (AU))	60
Figure 34.	35 mm, 17.5 mm and 8.75 mm crystal	61
Figure 35.	Four crystal (left) and five crystal (left) profiles	62
Figure 36.	Profiles of final pulse shape after six crystal stack (Horizontal axes Time (ps), Vertical Axes Intensity (AU))	62
Figure 37.	Three final profiles, each an average of 10 single shot pulse profiles.....	63
Figure 38.	Three simulations with crystal misalignments. Left: $\Delta\theta_1 = -2^\circ$, $\Delta\theta_2 = +2^\circ$, $\Delta\theta_3 = -2^\circ$. Center: $\Delta\theta_1 = +3^\circ$, $\Delta\theta_2 = -4^\circ$, $\Delta\theta_3 = -2^\circ$, $\Delta\theta_4 = +2^\circ$. Right: $\Delta\theta_1 = -2^\circ$, $\Delta\theta_2 = -4^\circ$, $\Delta\theta_3 = -2^\circ$	64

LIST OF TABLES

Table 1.	Characteristics of output optical pulses for typical sources and NGLS. After [23]	18
Table 2.	Power loss through crystals	48

THIS PAGE INTENTIONALLY LEFT BLANK

LIST OF ACRONYMS AND ABBREVIATIONS

GeV	Giga-Electron-Volt
MeV	Mega-Electron-Volt
KeV	Kilo-Electron-Volt
SR	Synchrotron Radiation
mrad	Milliradian
mm	Millimeter
cm	Centimeter
nm	Nanometer
μm	Micrometer
s	Second
ps	Picosecond
fs	Femtosecond
as	Attosecond
FWHM	Full Width Half Maximum
VUV	Vacuum UltraViolet
UV	Ultra Violet
FEL	Free Electron Laser
QE	Quantum Efficiency
nC	Nano-Coulomb
pC	Pico-Coulomb
RF	Radio Frequency
NCRF	Normal Conducting Radio Frequency
SCRF	Super Conducting Radio Frequency

kV	Kilovolt
DC	Direct Current
LINAC	Linear Accelerator
SASE	Self-Amplified Spontaneous Emission
NGLS	Next Generation Light Source
LBNL	Lawrence Berkeley National Lab
Hz	Hertz
kHz	kilo-Hertz
LCLS	Linear Coherent Light Source
nJ	Nanojoule
APEX	Advanced Photoinjector Experiment
CW	Continuous Wave
GVD	Group Velocity Dispersion
LLNL	Lawrence Livermore National Lab
LBO	Lithium Triborate
BBO	Barium Borate
OA	Optical Axis
RMS	Root Mean Square
PSC	Pulse Stacking Code
OPD	Optical Path Difference
UVFS	Ultra Violet Grade Fused Silica
MCP	Micro-Channel Plate
AU	Arbitrary Units

ACKNOWLEDGMENTS

I would like to first thank Prof. Bill Colson, Prof. Keith Cohn, and Prof. Joe Blau and all members of the FEL group at the Naval Postgraduate School for their help and support in this endeavor.

Secondly, I want to thank Dr. Fernando Sannibale and Dr. Daniele Filippetto at Lawrence Berkeley National Laboratory for their help, patience, and understanding as I worked and broke my way through the thesis.

Finally, I would like to thank my parents, Ed and Bernadette, and my brother Edward for their words of encouragement.

THIS PAGE INTENTIONALLY LEFT BLANK

I. INTRODUCTION

A. EVOLUTION OF LIGHT SOURCES

Alfred Lienard originally theorized Synchrotron Radiation (SR) in the 19th century, though it was not observed until 1945. It was first noticed as a bright light shining through the glass wall of an accelerating tube of a 70 MeV synchrotron at GE [1]. It took until the 1970s for it to become recognized as a scientific tool and now it is widely utilized across many different fields of study. SR comes from the transverse acceleration of a relativistic electron beam as it passes through a magnetic field. One characteristic of SR that makes it so viable as a light source is that the light is emitted in a forward facing cone with an approximate divergence angle (

tunable region of the electromagnetic spectrum. This increase in brightness characterized the 3rd generation of light sources. The brightness is defined as the number of photons (in 0.1% of the optical bandwidth) per volume per solid angle (units of photons / s·mm²·mrad²).

Important factors in determining brightness are the intrinsic properties of the electron beam. One such property is the electron beam's transverse geometric emittance. It depends on the product of the beam's transverse size and angular divergence,

$$\varepsilon_i = \sigma_i \sigma'_i, \quad (I.2)$$

where

where

with each material. From these patterns the structure of the material can be deciphered [7]. Another technique, known as X-ray absorption spectroscopy, can be used to probe the structures of different types of materials, by measuring the X-ray absorption in the sample as a function of the energy of the incident X-rays [8]. The size of the structures that can be probed scales with the X-ray wavelength used. As the push to shorter wavelengths goes forward, new types of experiments will be able to study even smaller structures.

II. FOURTH GENERATION LIGHT SOURCES

To increase the overall brightness and coherence of SR X-rays, the next generation of light sources is based on linear accelerators and FELs. The first FEL amplifier was demonstrated in 1976 at Stanford University and initially lased at 10 μm wavelength. Since then, FELs have become a widely used tool for creating tunable radiation [9]. The FEL is a true laser in that it produces coherent, nearly monochromatic light, but by a very different method compared to conventional lasers. This chapter will go into the components of 4th generation light sources as well as the physics behind them.

A. COMPONENTS

A typical laser uses a “pumping” mechanism to promote electrons to excited energy levels in a large portion of the atoms or molecules in the gain medium. Then the excited electrons drop down to a lower energy state, emitting light in the presence of radiation in a process known as “stimulated emission”. This group of coherent and monochromatic photons creates the laser beam. The FEL differs in that it uses a relativistic electron beam as the gain medium rather than crystals, dyes, gases or chemicals.

1. Electron Beam Generation / Injector

The electron beam consists of a series of bunches, typically millimeter long, separated by 10 m. The electron bunches can be supplied by several different types of sources. The sources generally contain two major components; a cathode device to generate the electrons and an accelerating cavity to rapidly accelerate the bunch once created. Combined, these two parts are often referred to as an injector or “electron gun” and is shown in Figure 1.

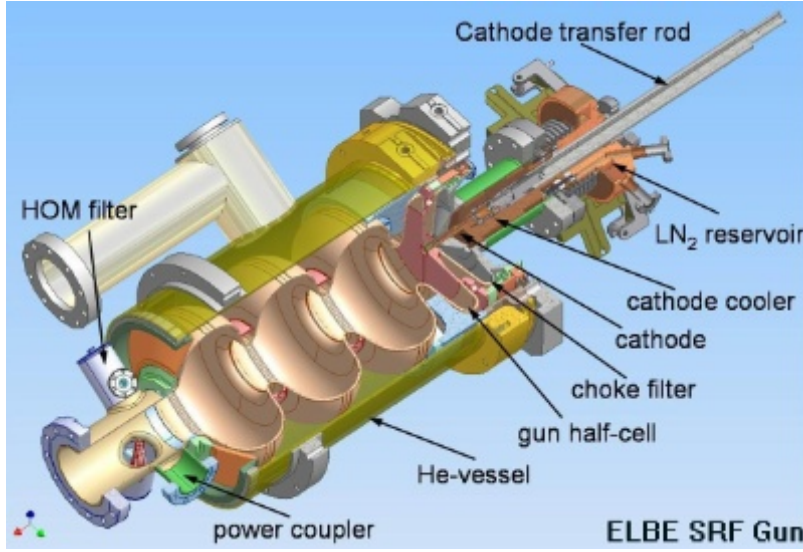


Figure 1. Schematic of 3 ½ cell RF photoinjector. From [10].

After creation from the cathode, the electrons repel each other due to Coulomb repulsion; this is often referred to as “space charge forces”. Once the electrons achieve sufficiently high energy, the space charge forces are mitigated via relativistic effects. The cathode is generally at one end of an accelerating cavity. This cavity supplies an electric field to rapidly accelerate the low energy bunch down the beam pipe before the space charge forces ruin the shape of the electron beam and increase the emittance.

a. Cathodes

The most widely used cathode for high brightness electron guns is the photocathode. It supplies high brightness electron beams and allows for emittance control during electron beam generation. It works based on the widely known photo-electric effect, where electrons are emitted by a material due to absorption of energy from incident photons. To release electrons in such a controlled manner a “drive laser” is used to supply the electromagnetic radiation. The laser delivers photons of sufficient energy onto the cathode where the interaction with the material then releases photoelectrons. The quantum efficiency (QE) of a cathode describes the number of emitted electrons per number of incident photons. A higher QE for a cathode material means that a lower number of photons is required to achieve the same emitted current. This requires less laser power from the drive laser. Some types of cathode materials consist of simple

metals such as copper, though they can also be semiconductors [11]. Photocathodes are able to supply bunch charges as large as 1 nano-coulomb (nC), though care must be taken when approaching such large values. In the high charge regime, space charge forces become more prevalent and can quickly degrade the emittance of the electron beam.

b. Accelerating Cavity

Accelerating cavities are a key component of the FEL. Most cavities are fed with radio frequency (RF) power that creates an alternating electric field inside the cavity that accelerates the electrons longitudinally down the beam pipe. Since the electric field alternates directions, the drive laser pulses must be timed correctly to generate electrons at the cathode only when there is the correct direction to the electric field. The RF frequency determines the spacing between the subsequent electron bunches and the diameter of the RF cavity. The RF fields that accelerate the free electrons cause ohmic heating in the cavity walls. This heat needs to be removed for the cavity to remain working properly. For a normal conducting RF (NCRF) injector a water jacket around a copper cavity is used to remove heat. For a lower RF frequency the cavity is larger, causing the power density in the walls to be lower. For higher frequency, and therefore smaller cavities, more advanced cooling is needed.

One method of heat mitigation of a higher frequency cavity is to build the cavity out of a superconducting material. The cavity is surrounded by a liquid helium ($\sim 3^\circ$ Kelvin) bath (cryostat), and becomes a superconducting RF (SCRF) cavity. When the cavity walls are superconducting the ohmic losses in the walls are greatly reduced. This gives several improvements over the NCRF version as the amount of RF power needed is greatly reduced and higher frequencies can be reached. However, the superconducting cavity makes it more difficult to utilize a magnetic solenoid near the cathode to aid in emittance control. In addition, the SCRF cavity increases the overall complexity by the addition of a cryostat.

After the initial cavity is used to accelerate electrons away from the cathode, a sequence of multiple cavities can accelerate the electrons up to higher

energies, as seen in Figure 1. The electron beam energy immediately after the injector is generally on the order of hundreds of kilovolts (kV) and is not quite relativistic.

Other types of injectors use a stationary electric field rather than RF. These “Direct Current” (DC) guns supply a constant longitudinal electric field gradient up to hundreds of kVs to accelerate the electrons. The electrons generated at the cathode are then accelerated towards the anode, a plate with a hole in the middle to allow the passage of the electrons. This type of gun is a relatively simple in design. The main concern for DC guns is designing the insulators so there is no voltage break down between the anode and the cathode.

2. Linear Accelerators (LINACs)

Once the electrons are created and accelerated out of the injector cavity, they may be accelerated to even higher energies for the FEL interaction. A linear arrangement of accelerating RF cavities (LINACs) can take electrons to kinetic energies from a few MeV up to many GeV. The LINAC operates on the same principal as the initial injector cavity. In both cases, the RF cavities use a mode that has a longitudinal electric field surrounded by a transverse magnetic field. Figure 2 shows an example of the direction of the fields in a typical cavity cross-section.

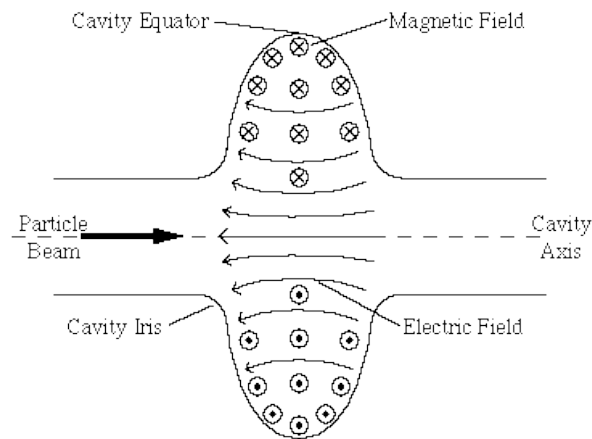


Figure 2. Cross-Section of generic cavity showing longitudinal E-field and transverse B-field (TM₀₁ mode). From [12].

An injector will generally have between one and three accelerating cavities, whereas the number of cavities in the LINAC is ultimately decided by the final energy desired for the electron beam. Just like the cavities for the injector, different schemes are utilized in designing LINAC sections including SCRF and NCRF LINACs as well as different shaped cavities. The final energy of the electron beam is important for the desired application of the FEL. To generate shorter X-ray wavelengths, higher energy electron beams are needed.

3. Undulator

The permanent magnet undulator contains two rows of permanent magnets, one on either side of the beam pipe. The magnets in each row have alternating poles so that they create a periodic magnetic field in the beam pipe as seen in Figure 3. The Lorentz force causes the electron bunches to oscillate back and forth in the transverse direction while traveling through the undulator.

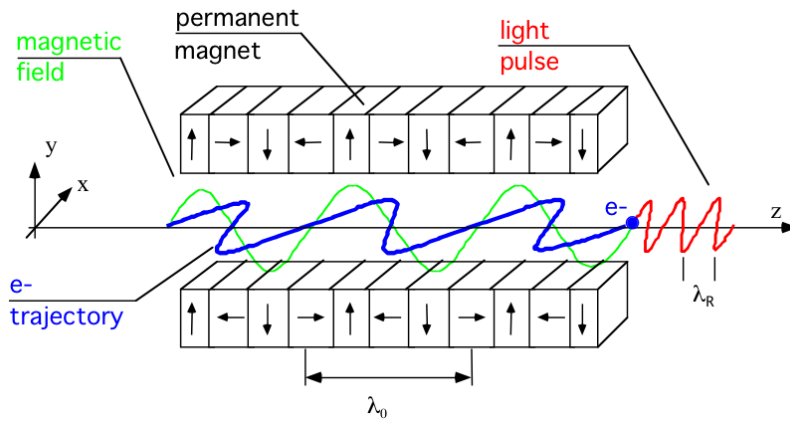


Figure 3. Schematic of linear undulator setup causing transverse electron oscillation. From [13].

The oscillating electrons act as a gain medium that generates and amplifies light. This is the same structure that was placed into storage rings of the 3rd generation.

In the FEL “oscillator” configuration two mirrors are placed on either end of the undulator creating an optical cavity. As SR is produced from the periodic acceleration of the electrons, the light is stored in the optical cavity. It is the interaction between the laser light and the oscillating electron beam that transfers energy into the optical beam.

As the optical pulse continues to propagate back and forth in the optical cavity it continues to interact with subsequent electron bunches. The power in the optical field grows over many passes through the undulator section. A fraction of the light's energy is released through a partially transmissive mirror, known as the "output coupler", at one end of the optical cavity.

In another setup, the FEL "amplifier" configuration has no optical cavity. Rather, there is a long undulator that the light and the electrons pass through just once. It is over this long length that the necessary interaction takes place. Typically a "seed laser" is used to provide the initial EM radiation that is then amplified by the FEL interaction. For a sufficiently long undulator, Self-Amplified Spontaneous Emission (SASE) can occur where the SR generated at the beginning of the undulator is amplified by the electrons in the remaining portion of the undulator. Both methods have their advantages and disadvantages, for example SASE does not require a seed laser, but it produces an optical beam with a poor temporal coherence. Other methods of "self-seeding" X-ray FEL's have been proposed to overcome the limitations of SASE FELs [14].

4. Beam Control

Various devices are used throughout the beam line to control the movement, position and shape of the electron beam on its way to the undulator. Dipole magnets supply a transverse magnetic field to bend the electron beam path. Chicanes (sets of 2 or more dipoles) can be used to bunch the electron beam longitudinally by altering the path length traveled by electrons of different energies. A quadrupole is a set of 4 magnets configured with alternating poles directed towards the center. Quadrupole triplets (3 quadrupole magnets in succession) are used to focus the electron beam in both transverse directions. RF cavity "bunchers" are used to bunch the beam longitudinally, by properly timing of the electron bunch arrival and the RF field inside a single cavity.

B. FEL INTERACTION

The physics behind the FEL process is in the interaction between the electrons, the periodic magnetic field, and fields of the optical wave.

1. Resonance Condition

For significant energy transfer between an electron and the optical field, the electron should travel through one period of the undulator as one optical wavelength passes over it. This has been coined as the “electron-photon” race and is illustrated in Figure 4. The electron is shown as the red dot, one optical wavelength (λ) is blue, while one undulator period is green (λ_0).

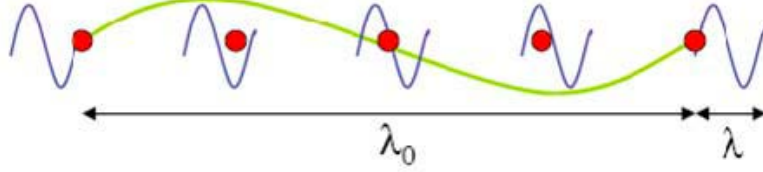


Figure 4. Schematic of “electron-photon” race. From [15].

One wavelength of light is emitted as the electron travels through one undulator period. The difference in their velocities is simply

$$\Delta v = c(1 - \beta_z) \quad (\text{II.1})$$

where $\beta_z = v_z/c$, c is the speed of light in vacuum and v_z is the electron longitudinal velocity. Multiplying this velocity difference by the time it takes the electron to transit one period of the undulator, $\Delta t = \lambda_0 / c\beta_z$, gives the wavelength of light λ , the “winning” distance.

$$\lambda = \Delta v \Delta t = c(1 - \beta_z) \cdot \frac{\lambda_0}{c\beta_z} , \quad (\text{II.2})$$

$$\lambda = \lambda_0 \frac{(1 - \beta_z)}{\beta_z} . \quad (\text{II.3})$$

This is “exact” resonance. For relativistic electrons, β_z is simply related to the Lorentz factor γ by

$$K = \frac{eB_{RMS}\lambda_o}{2\pi m_e c^2} . \quad (II.5)$$

Here, m_e is the mass of the electron, e is the electron charge magnitude and B_{RMS} is the root-mean-squared value of the magnetic field in the undulator. Using this relation Eq. II.4 becomes

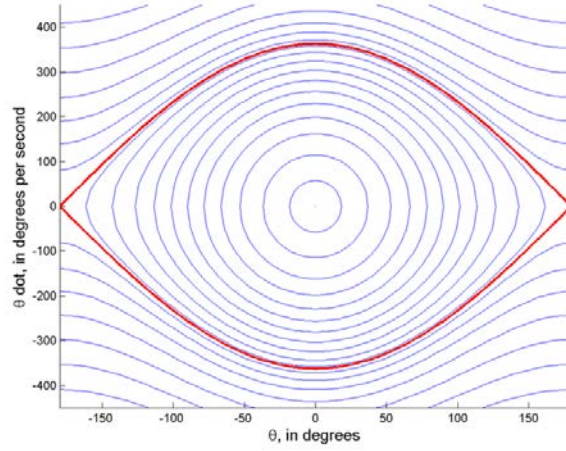


Figure 5. Phase space plot of simple pendulum. From [16].

Phase space is a useful tool as it shows the pendulum's phase velocity as a function of the position θ_p . As the pendulum oscillates back and forth, its phase, or angular, velocity and angle oscillate. In one full oscillation, a pendulum would sweep out one full phase space path. There are 3 types of phase space paths that are of interest, open orbit, closed orbit, and the “separatrix”. The separatrix (red path in Figure 5) is the special case that represents the pendulum having just enough energy to get to the top of the orbit ($\sim 180^\circ$) before falling back and rotating to the top in the other direction ($\sim -180^\circ$). Closed orbits represent a pendulum oscillating with an angle that never gets above 180° (vertical) causing the velocity to change sign along with the angle in one full period (blue ellipsoidal paths inside the separatrix in Figure 5). Open orbits represent the motion for a pendulum that has enough energy to continue around in a continuous circle, never changing directions as it sweeps out the phase space path (paths outside the separatrix in Figure 5). With this tool, the FEL interaction can be more easily understood.

3. FEL Pendulum Equation, Microscopic Electron Evolution

The microscopic evolution of an electron can be calculated using the relativistic Lorentz force law to describe the interaction between the electron, the undulator magnetic fields, and optical electromagnetic fields. It is easier to consider a helical undulator with the electron entering the undulator into a perfect helical orbit. The electron beam is

considered to be relativistic ($\beta_z \approx 1$). To describe the electron's microscopic phase with respect to the undulator and the optical fields introduce the electron phase,

$$\nu = \zeta = |a| \cos(\zeta + \phi)$$

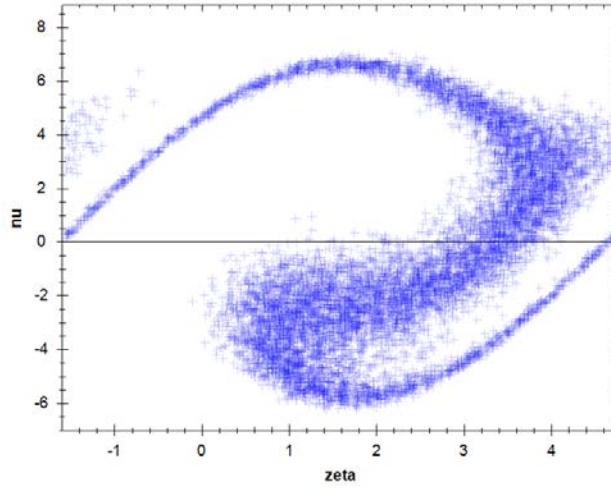


Figure 6. Shows a typical phase space plot for the FEL interaction. Each “+” represents the final phase space coordinate (ζ, ν) of an electron.

The electron phase velocity v is proportional to the electron's energy away from the resonant energy

time with respect to the optical period. With these approximations as well as neglecting diffraction and assuming the two beams overlap exactly, the wave equation can be written as

$$\ddot{a} = -j\langle e^{-i\zeta} \rangle. \quad (\text{II.11})$$

Here

III. THE NEXT GENERATION LIGHT SOURCE (NGLS)

Many fourth generation light sources have been proposed or are under development around the world [19]. The first source, LCLS, has achieved success with a moderate repetition rate ($\sim 100\text{Hz}$) of intense, coherent X-ray pulses at wavelengths down to $\sim 1\text{\AA}$ with pulse durations of $\sim 60\text{ fs}$ [20]. Lawrence Berkeley National Lab (LBNL) is pushing forward ideas for an X-ray laser that would give a much higher rate - up to hundreds of kHz - with pulse durations from attoseconds to femtoseconds. This would open the doors for a wide range of scientific experiments that deal with studying physical processes on these time scales. This pulse duration is nearly the same as the time scales for electron interactions in the valence shell of atoms and molecules, and would allow for these processes to be studied directly [21]. The “Next Generation Light Source” (NGLS) is the proposed 4th generation light source at LBNL[22]. This high repetition rate X-ray FEL would be a “user facility” supplying X-ray pulses to a number of sample stations. As seen in Figure 7, this type of undulator “farm” would be fed from one electron beam line. This beam line would include a beam transport and a switching section where the electron bunches would be directed down individual undulator beam lines, where each undulator could be tuned to a different wavelength range. This puts a large burden on the injector and accelerating sections to supply a high rate of electron bunches to all of the undulators.

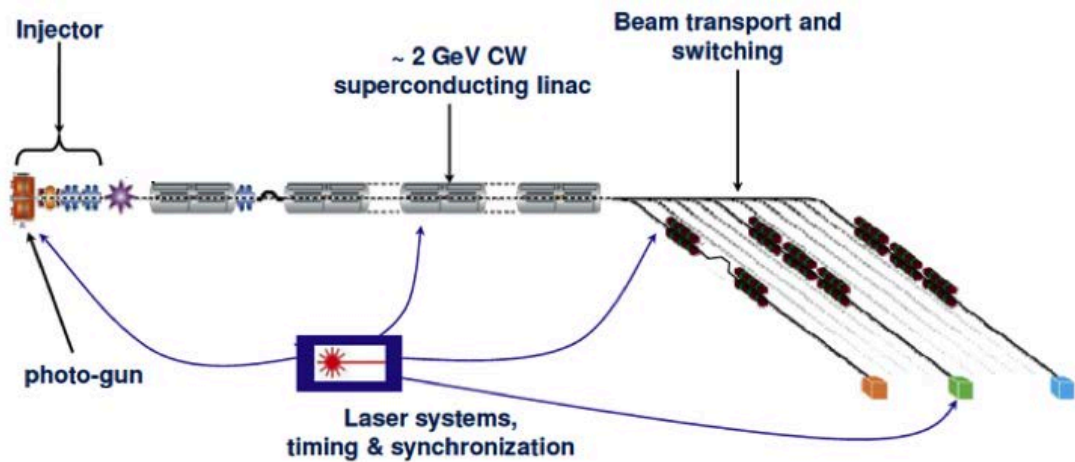


Figure 7. Schematic of NGLS proposed layout. After [24]

NGLS is at a research and development (R&D) stage to determine if the technologies needed to create such a device are feasible. Some of the parameters for 4th generation sources are listed in Table 1.

	Repetition Rate	Energy/micropulse	Pulse Duration
X-ray Storage Rings	GHz	$\sim \text{nJ}$ (10^{-9}J)	ps (10^{-12}s)
Current 4th generation X-ray laser sources	kHz	$\sim \text{mJ}$ (10^{-3}J)	$\sim \text{fs}$ (10^{-15}s)
NGLS	MHz	$\sim \text{mJ}$ (10^{-3}J)	$\sim \text{as-fs}$ ($10^{-18}\text{s} - 10^{-15}\text{s}$)

Table 1. Characteristics of output optical pulses for typical sources and NGLS. After [23]

NGLS bridges the gap between 3rd generation and the current 4th generation sources in terms of the repetition rate while matching current 4th generation sources in the energy per micropulse. To drive this high repetition rate, the FEL requires a photo-injector that can supply pulses at that high repetition rate and high beam quality that are needed for generating X-rays.

A. BASIC DESIGN

NGLS must be fed by a high repetition rate photo-injector running at the MHz level. It will have an accelerating section to reach an energy of ~ 2 GeV. Once the final energy is reached, a set of dipole “kicker” magnets deflects the electron bunches into separate beamlines leading to separate undulators. The different undulators are designed to supply specific X-rays for different types of experiments at various end-station labs.

B. INJECTOR

An injector capable of producing the necessary high repetition rate, beam quality, and charge is still in development at LBNL. The Advanced Photo-injector Experiment (APEX) at LBNL is a crucial part of the R&D effort for NGLS. APEX is a normal conducting RF electron gun that is designed to run at VHF frequencies (186 MHz) in

“Continuous Wave” (CW) operation [24]. In CW operation the RF power is constantly being fed into the copper cavity. Usually this is not possible for NCRF guns due to the energy dissipation in the metallic cavity walls. In the case of APEX, the frequency is low enough and the cavities large enough, that the peak wall-power density will only be $\sim 25 \text{ W/cm}^2$ [24]. This heat is removed by a water jacket surrounding the cavity. Higher frequency RF cavities are much smaller with higher power density making cooling more difficult. Typically, the higher frequency guns are cycled on and off with a low duty factor to reduce the heat deposited in the walls.

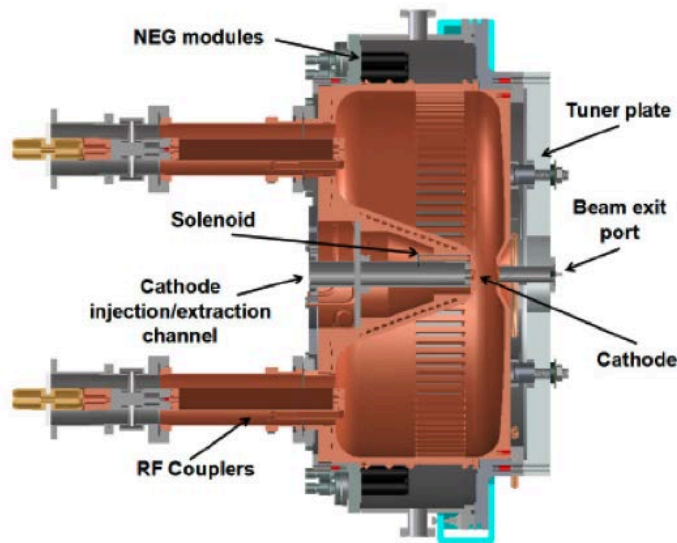


Figure 8. Cross Section of APEX design. From [25]

Figure 8 shows the major components of the APEX injector. There are two RF couplers to bring the RF power into the cavity, a focusing solenoid for emittance control of the early stages of the electron beam propagation, a “tuner plate” to mechanically alter the size of the cavity and tune the frequency of the cavity, and a large number of vacuum pumps (NEG modules). The cathode assembly will be attached using a “load-lock system” [26] so that the cathode can be removed from the gun without breaking the vacuum of the system.

Cathode technology is important for high brightness injectors and the cathode material for NGLS is still under research and development. The cathode used in this case

will be a photocathode, which emits electrons after being impinged by an intense laser pulse from the drive laser. The photo-cathode must be able to supply enough current while operating using present drive laser technology. This requires a cathode with a high QE, which comes with its own design and lifetime problems. Typically, high QE cathodes are easily contaminated and require excellent vacuum for a usable lifetime for the experiment. The APEX injector has a large number of vacuum ports to allow for excellent vacuum conductivity. This will allow the injector to operate at anticipated vacuum levels in the $\sim 10^{-11}$ Torr range. The long RF wavelength of the cavity (~ 1.6 meters) allows for large vacuum ports, increasing the vacuum conductivity, without disrupting the RF field [27].

IV. ELECTRON BEAM CREATION AND DYNAMICS

An important time in the electron bunch's lifecycle is when the electrons are at low energy just after being emitted near the cathode. At that time, the space charge forces can cause rapid emittance growth that degrades beam quality. After the electrons reach relativistic speeds, space charge effects are greatly reduced.

A. ELECTRON BEAM CREATION / PHOTOELECTRIC EFFECT

The photoelectric effect is the process by which electrons are emitted from a material due to absorption of photons. The energy of a photon (E_p) is directly proportional to its frequency (f_p) through Planck's constant (h) and is simply given by,

[29]. This regime is found to be an acceptable tradeoff between the bunch charge and the quality of the electron beam. The FEL gain is proportional to the “peak current” in the bunch and depends on the length of the electron bunch. This pushes for larger charge/bunch, but the space charge forces degrade the emittance as they are proportional to the bunch charge.

2. Bunch Shape

To decrease the space charge forces at the cathode while still maintaining a high charge/bunch, the electron bunch length is often made longer at the cathode than the final bunch length at the undulator. However, longer bunches sample more of the RF field of the accelerating sections, which can increase emittance and energy spread. When the electron bunch has high enough energy so that space charge effects have diminished, the pulse can then be compressed to increase the peak current. There are several compression schemes in the beam transport that ultimately end with a peak current high enough for the FEL interaction.

The overall electron bunch shape can also be designed to minimize the space charge forces, preserving the low emittance. An ellipsoid pulse shape is the theoretical ideal from the photocathode [30]. A uniform three-dimensional ellipsoid is the only shape where the internal forces between all of the electrons will be linear [31]. The space charge forces will still cause the bunch to expand, but do so equally in all directions. This type of expansion can be compensated by focusing coils along the beam line. With a photocathode, shaping the initial drive laser pulse can determine the shape of the electron bunch. To generate an ellipsoidal electron bunch, the longitudinal and transverse profile of the laser would have to be designed to create an ellipsoid with a constant photon density throughout. If the photon density were higher in one part of the laser pulse, the subsequent electron bunch would have a larger density in one area leading to non-linear space charge forces. This shaping is a difficult undertaking and usually a compromise is reached and the “beer can” profile is used. This shape is simply a right circular cylinder.

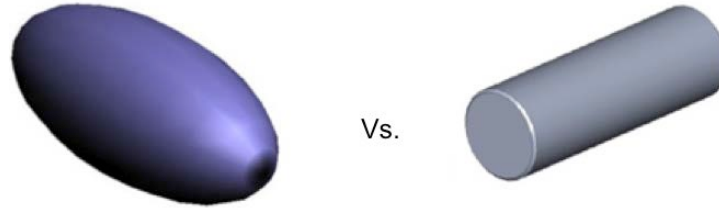


Figure 9. The ellipsoid vs. the cylindrical pulse shape

Figure 9 shows the two electron pulse shapes, but the creation of a cylindrical laser pulse with equal intensity throughout is more straightforward in practice. To shape a laser pulse involves two parts: the shaping of the spatial (transverse) dimension as well as the temporal (longitudinal) dimension. A method for doing this will be discussed in more depth in Chapter VI.

3. Emittance Matching

The photons also have a “geometric emittance” (ϵ_{gp}), which corresponds to the angular divergence and size of the optical beam. The radius of the optical beam follows the equation

To guarantee proper transfer of energy the electron beam should be within half of the optical beam radius as well as half of the angular spread. This leads to the condition for the electron beam emittance of

V. OPTICAL PROPERTIES

A. PROPERTIES OF LIGHT

1. Polarization

Many optical processes depend on the electric field orientation, or polarization, of the optical wave. As with any vector quantity, the electric field can be separated into two orthogonal component vectors. If the two components of the field are in phase, the field will oscillate in a single plane corresponding to the linearly polarized state. If the two components of the field are out of phase, then the components sum to a final vector that will change direction and amplitude in time, resulting in the elliptically polarized state.

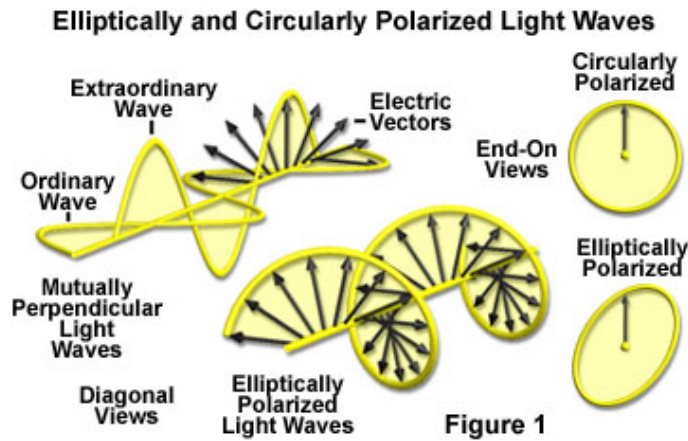


Figure 10. Depiction of elliptical and circular polarization [33]

In the latter case, the field sweeps out the shape of an ellipse in one period (Figure 10). A special case of elliptically polarized light occurs when the electric field components are out of phase by exactly 90° . In this case, the electric field's direction will change but the amplitude will always sum to the same value. This is called "circularly polarized" light.

2. Wave Packet

In continuous wave (CW) operation, the laser output has constant amplitude, whereas a pulsed laser system has a time component and can travel as a wave packet. A

pulsed laser has a group of frequencies that construct a beam envelope. Figure 11 shows a wave packet that is a superposition of waves with separate frequencies.

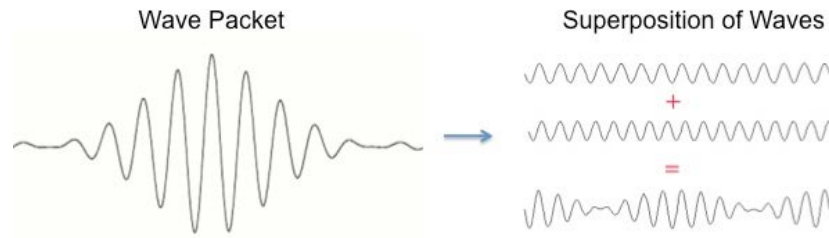


Figure 11. Demonstrates the wave packet as being a superposition of waves with separate frequencies. After [34]

When the laser propagates as a pulse, it takes a superposition of different frequency waves to create the wave packet. The range of different wavelengths needed describes the optical bandwidth of the laser pulse. Shorter pulse durations require more frequencies, i.e. wider bandwidth, to create the envelope. A short laser pulse has a frequency bandwidth that affects how the pulse interacts with different media.

B. REFRACTIVE INDEX

How an optical wave interacts with a medium is dependent on the medium's dielectric constant (ϵ). The velocity of light in vacuum can be calculated from the permittivity (ϵ_0) and permeability (μ_0) of free space,

In most optical materials the magnetic permeability (μ) is close to μ_o , leaving the relative electric permittivity as the only contributing factor. Optical components (mirrors, lenses, etc.) utilize a change in the refractive index to control the optical path of the light.

1. Dispersion

The velocity of light in a medium is dependent on its wavelength; equivalently, the refractive index of a material is dependent on the light's optical frequency. This difference in refractive index is called chromatic dispersion. A typical dispersion curve is seen in Figure 12, where it shows the index of refraction as a function of the wavelength of light. Different materials will have different dispersion curves.

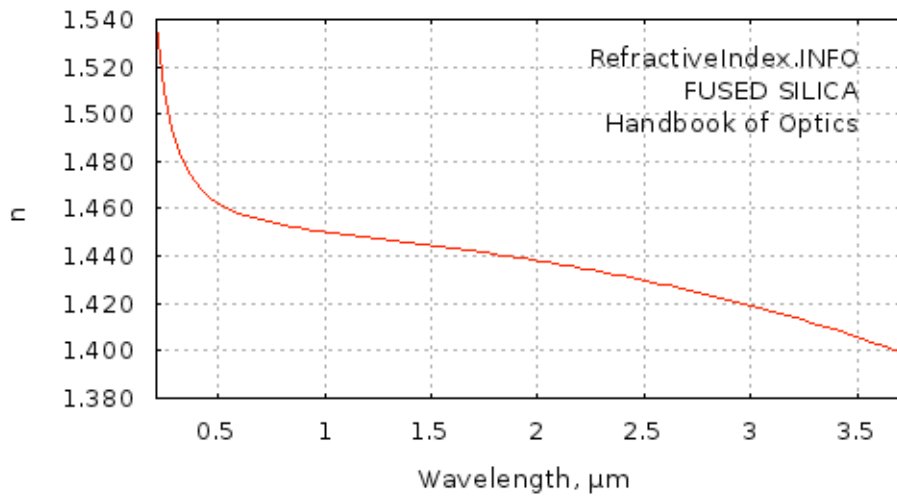


Figure 12. Dispersion curve showing the refractive index of Fused Silica as a function of wavelength. From [35]

The dispersion results in the pulse propagating at the “group velocity” in a material defined by

2. Birefringence

The refractive index of a material depends on the interaction of the optical field with the molecular structure of the medium. In an isotropic medium the refractive index is independent of the direction of propagation or the polarization of the incident light. Not all materials are isotropic; crystals are one example that can have anisotropic configurations, where the properties are non-uniform. This anisotropy can cause birefringence, where the light refracts differently depending on the polarization.

The birefringence of a crystal depends on the orientation and type of crystal lattice. The simplest case of a birefringent crystal is one of uniaxial anisotropy, where the structure of the crystal has one axis of symmetry, called the Optical Axis (OA) of the crystal. Uniaxial crystals will take the incoming light with any polarization and decompose it into two orthogonal components that are dependent on the crystal. One polarization will propagate through the material normally (following Snell's law) independent of the orientation of the polarization with respect to the optical axis; this is the ordinary polarization (o-wave) and has a refractive index n_o . The other component is the extraordinary polarization (e-wave) that has an index of refraction n_e , which is dependent on the orientation with respect to the optical axis [38]. The easiest way to picture this is by examining the refractive index ellipsoid shown in Figure 13.

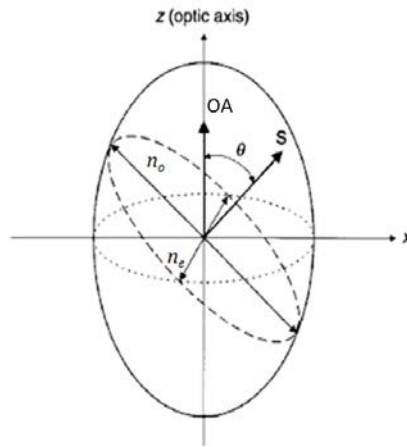


Figure 13. Index ellipsoid for uniaxial crystal depicting the polarization dependent refractive indices. This shows the propagation direction S , the optical axis OA , the polarization of the o-wave (n_o), and the polarization of the e-wave (n_e). After [39]

The ellipsoid illustrates the refractive index, n_o and n_e , of each polarization depending on the direction of propagation. The magnitudes of the corresponding vectors in the figure are proportional to the refractive index for those polarizations. If the propagating light were incident to the crystal parallel to the OA ($\theta=0^\circ$) then both polarizations would see the same index of refraction (n_o) and there would be no birefringence. If the incident light were orthogonal to the OA ($\theta=90^\circ$), then the o-wave and e-wave components would propagate according to their respective indices. The magnitude of the birefringence is calculated by the difference in the refractive indices for each polarization. The polarization-dependent characteristics of birefringent crystals allow them to be used in many optical devices. For example, they can be used to manipulate the polarization of light by adjusting the phase difference between two component vectors of the optical electric field.

VI. APEX LASER PULSE SHAPING

The charge density of the electron beam is a key parameter for the FEL interaction. This is initially controlled at the injector and then can be adjusted by longitudinal pulse compression and transverse focusing techniques. One means of adjusting the initial charge density is by controlling the shape and energy of the drive laser pulse.

A. LASER PULSE LENGTH

The drive laser is designed to generate photo-electron bunches of proper shape and at the correct RF phase to minimize emittance. The length of the initial electron bunch is directly related to the length of the drive laser pulse. The electrons need to be generated near the peak of the RF field to utilize the maximum accelerating field (V_{RF}). A rapid acceleration of the electrons decreases the time that space charge forces can affect the electron bunch. A short pulse of a given energy results in a short electron bunch and a high charge density. This is depicted in Figure 14.

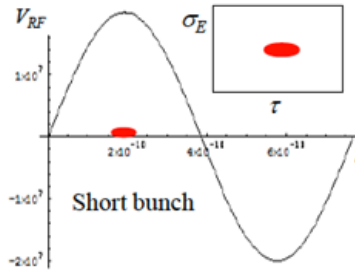


Figure 14. Illustration of accelerating gradient magnitude and short electron bunch length. From [25]

This illustration shows the magnitude of the accelerating gradient as a function of time through one RF period with the length of an arbitrary short electron bunch (red ellipsoid) for comparison. In this short bunch situation, the entire electron bunch is accelerated by approximately the same RF field, which has the benefit of decreasing the energy spread in the bunch. This is depicted in Figure 14 as the plot of

small energy spread and a high charge density that is needed for the FEL interaction, the Coulomb forces due to the charge density can degrade the emittance of the low energy electron bunch.

To mitigate this problem a longer initial electron bunch can be used as seen in Figure 15.

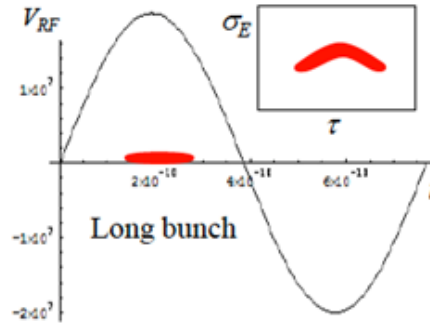


Figure 15. Illustration of accelerating gradient magnitude and long electron bunch length. From [25]

While the longer bunch aids in the mitigation of the Coulomb forces, if the electron bunch is too long relative to the RF period, the electron bunch will sample different accelerating fields, inducing an energy spread and leading to increased longitudinal emittance. This is depicted in the plot of

rate of ~37 MHz and a wavelength of 1054 nm. An acousto-optic device selects only 1 out of 37 pulses, reducing the frequency to 1 MHz. Then, the pulses are directed through four pre-amplifiers, where the pulses are stretched temporally while gaining energy from a diode laser pump source. The pulses are then coupled into a final fiber amplifier which brings the pulses up to their full power. After the final amplifier, the energy per pulse is at a maximum but dispersion has caused a temporal spread in the pulse due to the distance that the pulse has travelled in optical fibers. The 1054 nm wavelength is not usable for the cathode materials that are being used in the APEX project. To create shorter wavelengths a harmonic generation process is used which requires a high peak power.

To temporally compress the laser pulse a pair of diffraction gratings [40] is used which brings the pulse to a length of ~0.6 ps FWHM with ~1 MW of peak power (~0.72 μ J per pulse) [41]. To generate the second harmonic of the 1054 nm light, the pulse is focused through a Lithium Triborate (LBO) non-linear birefringent crystal. This converts the wavelength from 1054 nm to 529 nm light with ~400 kW of peak power (~0.25 μ J per pulse). The efficiency of the harmonic generation process depends on the type of non-linear crystal, the length of the crystal, the focal length of the laser pulse as well as other parameters [42]. Since different cathode materials will require different energy photons, either the 529 nm light can be directed to the cathode or it can undergo another harmonic generation process to generate even higher energy photons. To generate the fourth harmonic, the beam is focused through a β -Borium Borate (β -BBO) non-linear birefringent crystal to produce a 264 nm (UV) wavelength beam with ~130 kW of peak power (~0.08 μ J per pulse) [41]. A schematic of the laser is show in Figure 16.

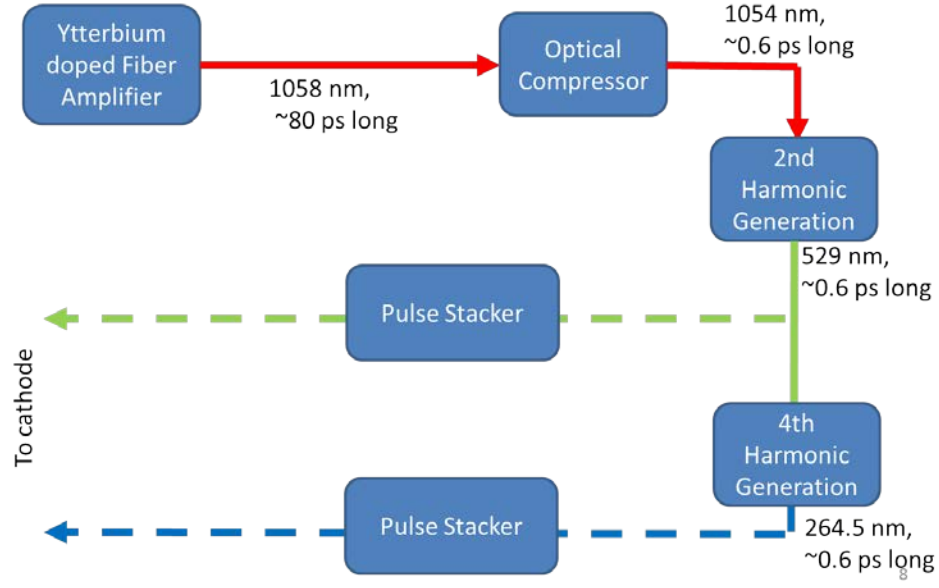


Figure 16. Schematic of APEX drive laser

With an RF period lasting ~ 5.4 ns, a ~ 0.6 ps laser pulse duration from the drive laser is a small fraction of the RF cycle. This is the case that was shown in Figure 14, where the bunch will have a small energy spread but Coulomb forces may degrade the emittance. Simulations of the electron beam show that a pulse length of ~ 60 ps is small enough compared to the long RF period and long enough to help mitigate initial emittance growth while not requiring excessive compression later in the beam line [43]. This sets the approximate goals for the laser pulse shaping.

C. LASER PULSE SHAPING TECHNIQUE

To generate the “beer can” electron bunch shape that was discussed in Chapter 4, the initial laser pulse will need to be formed into a similar shape. To adjust the shape of the electron bunch, both the transverse as well as the longitudinal components of the pulse need to be controlled.

1. Transverse Pulse Shaping

To shape the transverse profile of the laser beam, an aperture is used to cut the laser beam into a circular profile. As the laser propagates through the aperture, the outer

edge of the laser beam is “scraped off”, leaving a circular portion in the middle. To generate a quasi-uniform photon density across the profile, the laser pulse is first expanded through a telescope to increase the transverse size before being cut by the aperture. Putting the pulse through a circular aperture produces Airy disks after diffraction, where a central peak intensity is surrounded radially by rings of lesser intensity. This is not desired, and has been shown to give worse emittance than the nominal circular transverse profile [44]. A way to avoid these rings is to image the exact plane of the aperture directly onto the cathode with a series of lenses. If done correctly this would allow for a circular profile at the cathode.

2. Longitudinal Pulse Shaping

After the β -BBO crystal, the laser pulse has a longitudinal Gaussian profile with a FWHM of ~ 0.6 ps. The APEX project requires this to be elongated by a factor of approximately one hundred to ~ 60 ps, while maintaining the rise and fall time of the initial pulse, ~ 1 ps. A set of birefringent crystals can be used to generate a longer pulse with these properties by separating the initial pulse into a number of temporally spaced “sub-pulses” [45]. Adjusting the lengths of individual crystals allows the separation distance between sub-pulses to be controlled. If controlled in the correct way, the amplitude of the individual sub-pulses sum together so that the overall pulse envelope is one of an approximate flat top as illustrated in Figure 17.

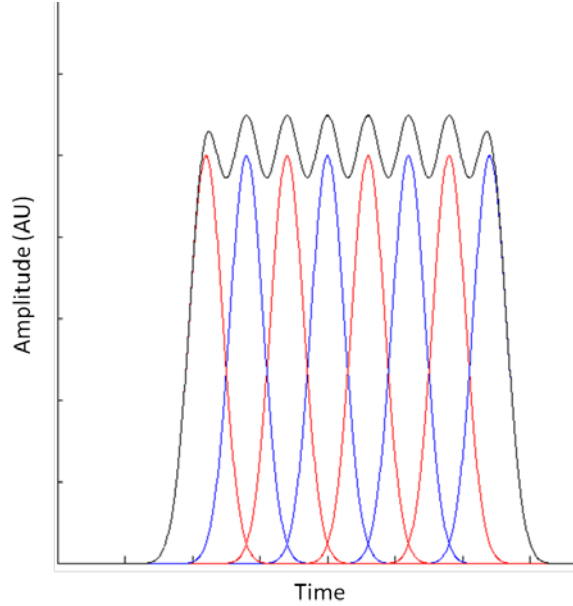
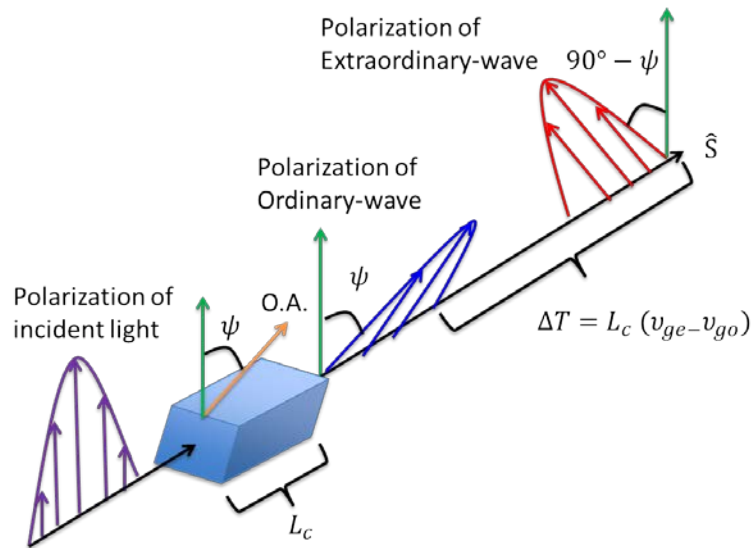


Figure 17. Illustrates summation of temporally spread Gaussians with alternating polarizations (denoted red and blue)

If a group of individual Gaussian pulses (blue and red) are equidistantly spread in time, the sum of the electric fields creates an approximate flat top envelope (black). The magnitude of the energy variations along the pulse envelope is directly related to the number of sub-pulses, the distances between subsequent sub-pulses, and the duration of the individual sub-pulses that construct the envelope. The amount of energy variation along the pulse needs to be kept small to prevent extraneous emittance growth from localized spikes in the electron density at the cathode. The mechanism for creating the subsequent sub-pulses causes the polarizations to alternate between neighboring sub-pulses, mitigating any constructive or destructive interference in the overlap region.

The birefringent crystals used for the pulse shaping have their optical axes (OA) parallel to the face of the crystal (commonly referred to as “a-cut”). This orientation between the OA and the propagation direction of the laser causes the crystals to shift one polarization temporally with respect to the other [46]. Each crystal splits every incident pulse into two “daughter” pulses with opposite polarization. How much one daughter pulse shifts with respect to the other is dependent on the length of the crystal as well as the difference in the group refractive index between the two components of the

polarizations projected onto the OA. This temporal shift (ΔT) is calculated from the length of the crystal and the difference in speed at which each component of the polarization propagates through it,



For this application, the pulse shaping technique is designed to split the initial laser pulse into a set number of pulses with equal amplitude and equal separation to generate an overall flat top envelope. An angle of $\psi=45^\circ$ with respect to the incident polarization splits the energy equally between the two daughter pulses [47]. To maintain equal separation between neighboring sub-pulses each crystal must follow the relation

V.8, for the desired wavelength using Eq. V.6. With this information, the amount of delay per unit length that each individual crystal will impart between subsequent sub-pulses is calculated.

The PSC tracks each individual pulse's interaction with a birefringent crystal. When a pulse interacts with a crystal, it is separated into two sub-pulses with the temporal spacing between them, ΔT , calculated from the crystal length and the delay factor determined by the crystal material properties, Eq. VI.1. The amplitudes of the sub-pulses are calculated depending on the angle between the initial laser pulse polarization and the crystal's OA, with the total energy of the sub-pulses equal to the energy of the initial pulse. The polarizations assigned to the two sub-pulses are parallel to (ordinary polarization) or orthogonal to (extraordinary polarization) the OA of the crystal. The laser pulse interacts with the crystals sequentially, tracking each sub-pulse's amplitude, polarization, and delay as the sub-pulses are created and propagate through the crystal stack. The PSC tracks each sub-pulse's interaction with the crystal before stepping forward and calculating the interaction with the next one. After the pulses have propagated through the N crystal stack there are 2^N sub-pulses, each with their own amplitude, position, and polarization.

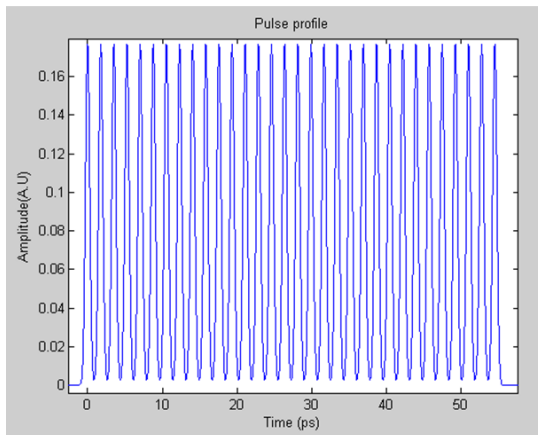
The code does not track the overall profile of the pulse as it transits the crystal stack, but rather tracks the parameters of the individual sub-pulses. After the interaction with the last crystal, the parameters of each sub-pulse (amplitude and location) are then summed, each with an assumed Gaussian profile of the initial pulse width. To check that the total energy of the system is conserved, the energies of each sub-pulse are summed and compared with the energy of the initial pulse.

E. CALCULATIONS

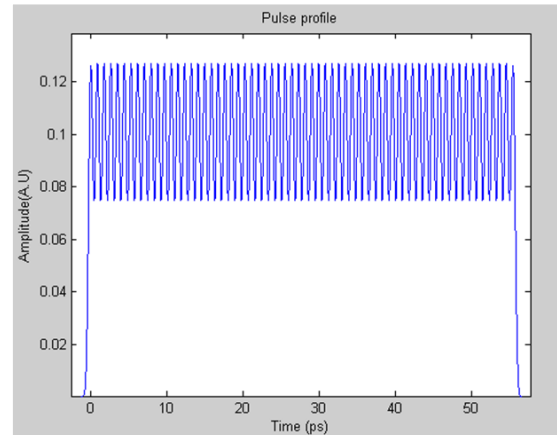
The maximum procurable length of the crystals leads to a final designed pulse length of ~56 ps. For the scope of this thesis, only the 264 nm (fourth harmonic) pulses were shaped for the APEX project. To transform the initial ~0.6 ps pulse into the final ~56 ps pulse with a flat top and sharp edges requires the total optical path difference (OPD) between the first and last sub-pulses after the crystal stack to be ~56 ps. This controls the sum total of crystal lengths that can be used for the pulse shaping. An α -

BBO birefringent crystal was chosen to do the pulse shaping of the UV laser pulse due to its large birefringence at the required wavelength as well as its high transmission coefficient in the UV. The Sellmeier equations for the refractive indices of the ordinary (n_o) and extraordinary (n_e) waves are

Overall Pulse envelope



5 crystals (32 pulses)



6 crystals (64 pulses)

Figure 19 plots the amplitude of the optical pulse against time for two cases. The first case uses 5 crystals to split an initial pulse into 32 sub-pulses, while the second uses 6 crystals for an additional split into 64 sub-pulses. The initial Gaussian pulse was assumed to have a FWHM of 0.6 ps to keep the ends of the “beer can” sufficiently flat. The crystal lengths were selected to be 35 mm, 17.5 mm, 8.75 mm, 4.375 mm, 2.1875 mm for the 5 crystal stack. An additional crystal of 1.0938 mm added for the six crystal stack. The maximum procurable crystal length of 35 mm made it so the only feasible difference between the two cases is the addition of a thinner crystal (which still followed Eq. VI.2). With the 5 crystal stack the overall beam envelope has an energy variation of ~100%, while the 6 crystal stack had an energy variation of only ~40%. These large energy variations are due to the extremely short initial pulse duration and the large amount of temporal expansion needed. To decrease the energy variation, either more crystals can be used to split the energy into more pulses or the initial pulse can be made longer.

The group velocity dispersion can be used to aid in decreasing the energy variation of the final pulse envelope. Before being separated into different sub-pulses, the initial Gaussian pulse can be spread temporally by directing the pulse through a dispersive medium. To calculate how much of an effect this will have, the optical bandwidth of the laser pulse is needed.

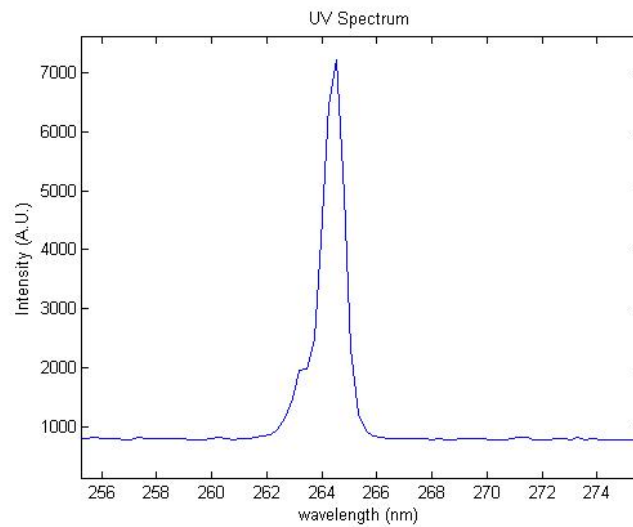


Figure 20. Measured UV spectrum of laser pulse

Figure 20 plots the intensity as a function of wavelength of the initial UV laser pulse, measured using an Ocean Optics HR4000 Spectrometer. The spectrum has a peak at 264.5 nm and a range of wavelengths from 263.85 nm to 264.92 nm (FWHM). The range of wavelengths ($\Delta\lambda$) and the optical frequency bandwidth (Δf) are related by

Overall Pulse envelope

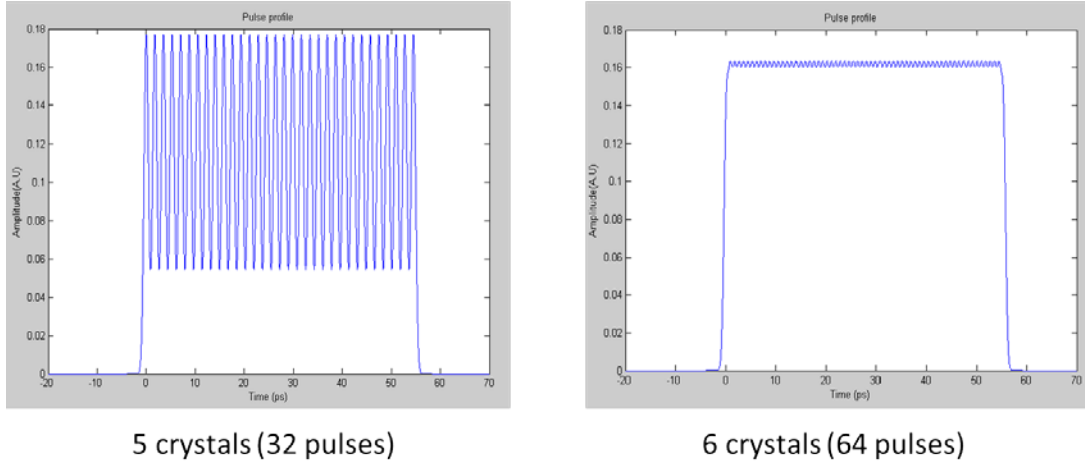


Figure 21. Longitudinal profiles from simulation (1.07 ps initial pulse)

If less variation is needed, other dispersive elements can be put in the laser's path before the crystal stack. The factors that must be considered when finding a different dispersive material are the GVD and absorption of the material at the desired wavelength. A lower GVD requires a longer length of material to produce the same temporal spread, which leads to power loss due to absorption and can significantly decrease the optical power at the cathode. Ultra Violet Grade Fused Silica (UVFS) works well for the target wavelength of 264 nm. Calculating the GVD from the dispersion curve for our peak wavelength gives a value of 199.6 fs²/mm. While this is a small amount of temporal spreading compared to the effect of the α -BBO it could still be utilized.

THIS PAGE INTENTIONALLY LEFT BLANK

VII. EXPERIMENT

A. INITIAL EXPERIMENTAL SETUP

1. Measuring Laser Polarization

Controlling and measuring the polarization of the laser pulse is important for aligning the crystals correctly. To measure the laser polarization, an optical component known as a “polarizing beam splitter” is used. It is composed of two identical halves of a UV Fused Silica cube, cut diagonally, that are bonded together with a barrier between them that has a different refractive index. The combination of this geometry and the discontinuity of the refractive index splits the incoming beam into two separate beams with orthogonal polarizations. A diagram of a polarizing beam splitter is shown in Figure 22.

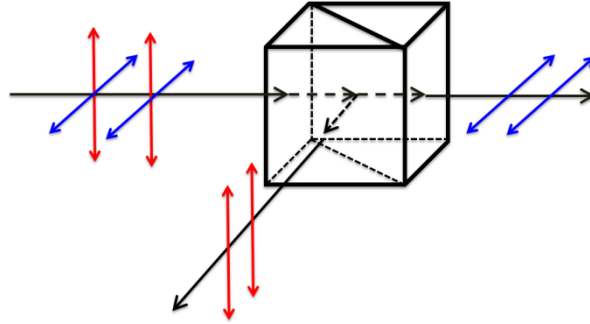


Figure 22. Diagram of polarizing beam splitter cube

In Figure 22, a beam consisting of two orthogonal polarizations (denoted blue and red) enters into the beam splitter from the left. Due to the difference in refractive index at the barrier in the middle of the beam splitter, part of the beam is reflected (red arrows) and part of the beam is transmitted (blue arrows), based on the laser pulse polarization. The incident polarization can be inferred by measuring what percentage of the initial power is transferred to the reflected and transmitted beams. For a linearly polarized beam, if the power is evenly distributed between the two output beams, then the laser pulse has its polarization 45° from the orientation of the polarizing beam splitter. If the power is

transferred only into one of the output beams, then the initial polarization is aligned with that particular orientation of the beam splitter. This is used to quantify the laser polarization.

2. Controlling Laser Polarization

To align the crystal's optical axis correctly the initial polarization of the laser pulse needs to be controlled. This alignment is done using a birefringent crystalline optic known as a "half wave-plate". It is a thin birefringent crystal with its Optical Axis (OA) aligned 90° from the laser propagation direction, in the same way as the α -BBO used for the pulse shaping. This optic works as a retarding plate and simply shifts the orientation of linearly polarized light by adjusting the phase difference between the orthogonal components of the wave's electric field. The thickness of the crystal causes one polarization to be shifted from the other by a distance of half of a wavelength. This allows the polarization to be controlled over the full 360° by adjusting the angle between the OA of the half wave-plate and the polarization of the incident light. The combination of the wave-plate and the polarizing beam splitter allows the polarization of the laser pulse to be adjusted and measured.

3. Initial Laser Polarization

The pulse stacker is designed to have six crystals, oriented so that the final sub-pulses have their polarizations either aligned with, or orthogonal to, the initial polarization. The final pulse's polarization is important in beam transport because the percentage of incident power that a dielectric mirror reflects is dependent on the polarization of the light. For this reason, the final pulse is desired to be made up of sub-pulses with their polarizations 45° from vertical. This allows each sub-pulse to have equal horizontal and vertical components to their polarization. Since each sub-pulse will have equal components, all of the sub-pulses will reflect in the same manner without distorting the wave-front, or decreasing power in any particular polarization [50]. This allows each sub-pulse to lose the same amount of energy after each reflection; otherwise, every other sub-pulse would lose more energy, thereby inducing a longitudinal energy variation in the final laser pulse. To guarantee that polarization is achieved, the initial

laser pulse needs to have its polarization adjusted so that it is 45° from the vertical using the means described earlier. For measurement purposes, aluminum mirrors will be utilized to direct the laser pulses to the streak camera. Aluminum mirrors do not have a polarization dependence on their reflectivity, unlike dielectric mirrors. This is useful when measuring the energy in individual sub-pulses to help align the crystals correctly.

4. Initial Crystal Alignment

The same wave-plate and polarizing beam splitter can be used to align each crystal's Optical Axis (OA) correctly with the polarization of the initial pulse. As was stated in Chapter 6, the first, third, and fifth crystals need to have their optical axes aligned 45° from the initial polarization. Each crystal is in a rotational mount that allows controlled, indexed rotation of 360° . As was outlined in the previous section, this first crystal's orientation will need to be in the vertical direction. This can be roughly aligned to within a couple degrees using the wave-plate and polarizing beam splitter. First, the initial laser pulse is oriented in the vertical direction using the wave-plate. The crystal that is being aligned is then inserted in the beam path between the wave-plate and the polarizing beam splitter. The crystal is rotated while viewing the power transmitted through the beam splitter, and when the power transmitted through the beam splitter is minimized, the laser pulse polarization is unchanged. This orientation causes the pulse to only interact with one of the refractive indices so there is no splitting of the pulse into two orthogonal sub-pulses. This means that the laser pulse's polarization is either parallel or orthogonal to the OA of the birefringent crystal. Either of these crystal orientations with respect to the initial polarization will produce the same effect as it maintains the 45° difference between the first crystal and the initial polarization as well as the 45° difference between subsequent crystals.

This same process is done for all six crystals individually. At this point all crystals have their axes aligned. The second, fourth, and sixth crystals are then rotated manually by 45° to correctly alternate the orientations. The initial polarization is then set to 45° with respect to the OA of the first crystal.

B. UV POWER LOSS

Power loss along the laser path is a major concern for the APEX drive laser. The amount of current created in the electron gun is directly related to the amount of laser power imparted on the cathode, so minimizing the loss through the beam line is important. The α -BBO crystal material was chosen for its transmission efficiency and birefringence in the UV. Table 2 shows the measured power losses due to each crystal length.

Crystal #	Crystal Length (mm)	% Reflected	% Absorbed
1	35	0.9%	4.9%
2	17.5	1.8%	3.4%
3	8.75	1.4%	3.4%
4	4.375	1.6%	2.1%
5	2.1875	1.6%	1.15%
6	1.09375	1.4%	2.3%

Table 2. Power loss through crystals

The power was measured before and after each crystal to characterize the loss. The total crystal stack leads to a total loss of ~28%. Correct alignment and anti-reflective coatings are important in mitigating power loss.

C. LONGITUDINAL PULSE SHAPE MEASUREMENT

Measuring the longitudinal profile of a laser pulse on the picosecond time scale is no small task. Photodiodes usually have response times that are too slow to measure a ~56 ps pulse. One device that is capable of measuring such short pulses is a streak camera. It provides a means for measuring the longitudinal profile of light pulses with temporal resolution down to ~2 picosecond level.

A streak camera is a device which translates the longitudinal properties of an optical pulse to a transverse profile that can be more easily measured. Its key components are depicted in Figure 23.

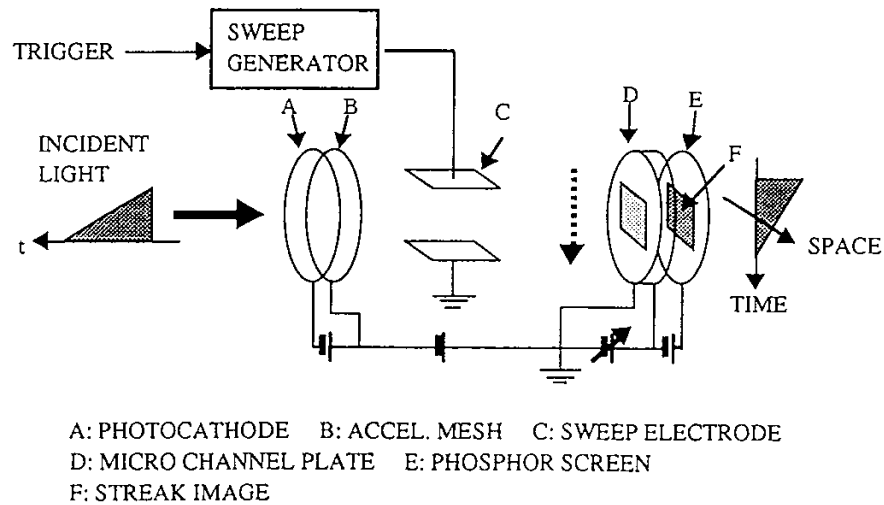


Figure 23. Diagram of key components of streak camera. From [51]

The incident optical pulse is initially imaged by a set of internal optics onto a photocathode (A) where it absorbs the photons from the laser pulse and produces an electron bunch with a length and density proportional to that of the initial laser pulse's length and intensity. This electron bunch is accelerated away from the photocathode by a wire mesh (B) that is held at a certain potential with respect to the cathode. This electron bunch then travels through free space between a pair of sweep electrodes (C). At a known time after the generation of the electrons, a trigger signal causes a ramping (increasing) voltage to be applied across the sweep electrodes. This causes different longitudinal components of the electron bunch to be deflected by different amounts, and converts the longitudinal information of the optical pulse to the transverse profile of the electron bunch. This electron bunch then travels through a micro-channel plate (D) that multiplies the number of electrons without disturbing the transverse position of the bunch. The amount of multiplication can be controlled to get a clear image. The bunch is then accelerated onto a phosphor screen (E) and creates an image of the transverse profile of the electron bunch. An analog camera is used to capture the image and transfer it to a computer for processing.

1. Sweep Unit

The Hamamatsu C5680 Streak Camera that is being used for this experiment has multiple interchangeable sweep modules which offer different types of sweep voltages for different operating regimes. There are single sweep units, which supply a linear sweep voltage across the electrodes, and “Synchroscan” units, which supply a constant sinusoidal sweeping voltage to the electrodes. The two waveforms are shown in Figure 24.

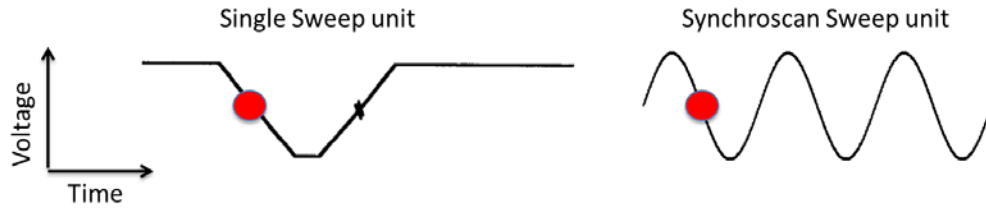


Figure 24. Different types of sweep voltages from Streak Camera. After [51]

Figure 24 depicts the necessary timing between the electron bunch (red circle) and the linear portion of the sweep voltage (black lines). For this experiment a Synchroscan sweep unit was used to measure the pulse from the APEX drive laser. This sweep unit is calibrated for a 125 MHz frequency, which must be synchronous with the 1 MHz frequency of the laser. If there is a mismatch in frequencies, then the position of the streak image on the phosphor screen will shift from pulse to pulse and won't allow consistent measurements.

The Synchroscan was calibrated to give a maximum resolution of <2 ps. The sinusoidal nature of the sweeping voltage leaves only a portion of the period with a linear trend, so the signal of the laser pulse must be timed to be in this portion of the period. The resolution of the streak camera can be adjusted by increasing the amplitude of the sweep voltage. This leaves the sweep period unaltered, but the portion of the period that correctly transfers the electrons onto the visible portion of the phosphor screen is shortened. Depending on the amplitude of the sweep voltage, the portion of the period transferred to the visible portion of the screen can be from ~ 1.4 ns to ~ 200 ps.

2. Operating Regimes

The streak camera can be operated in multiple regimes for processing the streak image. The streak camera can take single shot measurements, which will track the profiles of individual pulses, or it can use an averaging technique to create a smooth image from multiple shots. The latter is a clearer method for seeing the pulse shape, but requires the frequency of the Synchroscan unit and the incident laser to be closely matched with very low jitter between the signals. While the APEX drive laser is the 125th harmonic of the Synchroscan frequency, the arrival time of the laser pulse with respect to the 125 MHz signal varies on a shot to shot basis on the order of a hundred picoseconds. This is depicted in Figure 25.

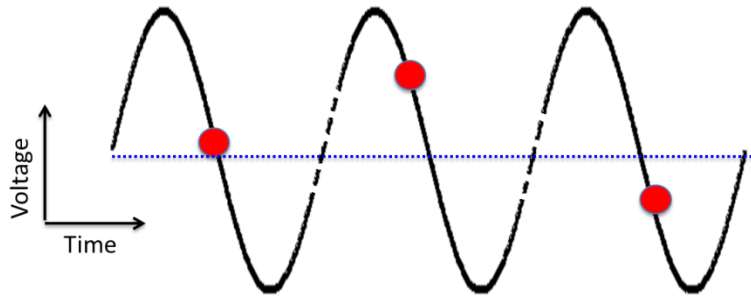


Figure 25. The jitter caused by the varying arrival time of the incident laser pulse

The jitter between the two signals causes subsequent electron bunches to interact with different portions of the sweep voltage. This causes the streak image to move vertically on the phosphor screen from shot to shot. Due to this constant movement, the averaging technique would artificially broaden the measured pulse length.

With a known sweep voltage time, the pulse duration can be determined by the vertical length of the image on the phosphor screen; the horizontal size on the screen corresponds to the optical pulse's transverse size. The brightness of the image is proportional to the intensity of the electron bunch and consequently the intensity of the laser pulse. A typical streak image and profile is shown in Figure 26.

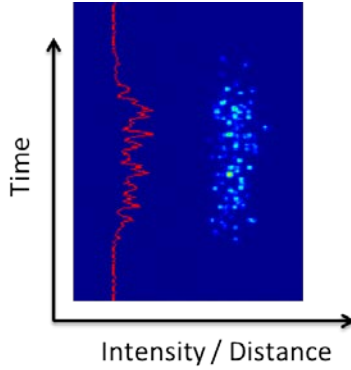


Figure 26. Streak image and profile analysis from Streak Camera

The streak image on the right of Figure 26 is a single-shot measurement that depicts the intensity of the electron bunch. The vertical axis corresponds to the time duration of the initial laser pulse while the horizontal axis corresponds to the transverse direction. The profile on the left is a depiction of the intensity of the pulse as a function of time.

To optimize the streak camera and decrease artificial broadening several steps can be taken in the setup for the measurement. The number of photons created at the photocathode of the streak camera needs to be kept small to avoid Coulomb forces from expanding the beam. This expansion would degrade the quality of the measurement by making the electron beam larger than the laser pulse. The micro-channel plate (MCP) can also be “gated” to only multiply electrons at certain points in the sweep period, which aids in negating signal from extraneous light entering the streak camera. To avoid a decrease in resolution the incident laser pulse is attenuated until an image is only viewable on the phosphor screen under moderate MCP gain, or amplification. This decreases the Coulomb forces after the photocathode while still supplying enough signal on the phosphor screen to make a measurement.

D. MEASUREMENT CAPABILITIES

The Hamamatsu C5680 streak camera is capable of measuring UV wavelengths if initially designed to do so, but it must have the correct photocathode and optical components for the desired wavelength. The streak camera that was available for this

experiment was initially acquired for the measurement of visible photons. Due to this, the internal optics that image the front slit of the streak camera onto the cathode were designed for these longer wavelengths. The UV wavelength is much shorter than the intended wavelength and generally has a larger refractive index in most optics. This difference in refractive index between the streak camera's designed wavelength and the one that is trying to be measured causes the light to not be imaged onto the photocathode correctly, so that the beam is not visible on the streak camera during operation.

The effect of the birefringent pulse stacker on a green laser pulse, while not the initial design wavelength, can still be used to infer the pulse stacker's ability to work in the UV. The a-cut birefringent crystals have a wavelength-dependent effect in two areas: the difference in the group velocities between the two polarizations, and the amount of individual pulse spreading due to group velocity dispersion. The angles between the laser pulse polarization and crystal's OA is constant among different wavelengths and the lengths of the individual crystals still generate equidistant pulses. The α -BBO had a delay factor (ΔT) of 0.804 ps/mm for the UV, leading to a final pulse length of ~56 ps from the six crystals with ~68 mm of total crystal length. The birefringence of the α -BBO is less for the green wavelength and leads to a delay factor of only 0.455 ps/mm. The combination of this new delay factor and the ~68 mm of crystal will lead to a final pulse length of ~32 ps, in the green.

The group velocity dispersion (GVD) in the α -BBO crystal for the 529 nm light is much smaller than the GVD for a UV pulse. This will cause the final length of the green individual pulse to not spread as much as the UV. Calculating this spreading from the measured spectrum using Eq. VI.6 and Eq. VI.7, the final green sub-pulse length after the crystal stack will remain ~0.6 ps.

Combining these two different factors into the simulation for the final pulse envelope creates a flat top similar to the UV and is depicted in Figure 27.

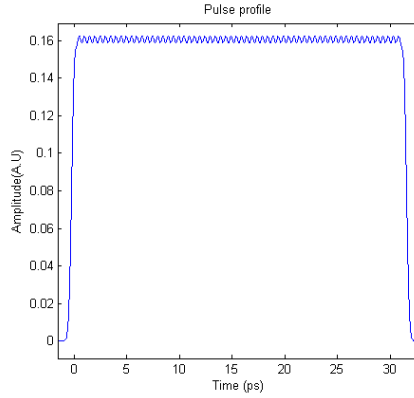


Figure 27. Simulation of pulse profile of green light shaped by six crystal pulse stacker

This differs from the six crystal profile seen in Figure 27 only by the overall pulse length while maintaining the same approximate energy variation. If the birefringent crystals control the green laser pulse in the manner predicted, then it can be concluded that the effect that the crystals would have on a UV laser pulse would also follow the prediction.

E. RESULTS

Although each crystal was closely aligned using the polarizing beam splitter and wave-plate, the final adjustment came from analyzing the streak camera data. Each crystal was put in place sequentially, starting with no crystal, then the first crystal (35 mm), second (17.5 mm), and so forth. After each crystal was placed, the angle of the optical axis was adjusted until the expected profile was obtained, as described below.

1. No Crystal

To demonstrate the resolution of the streak camera in the current set up for the experiment, the first measurement of the green laser pulse was with no crystal in place. This was taken as a single-shot measurement and is shown in Figure 28.

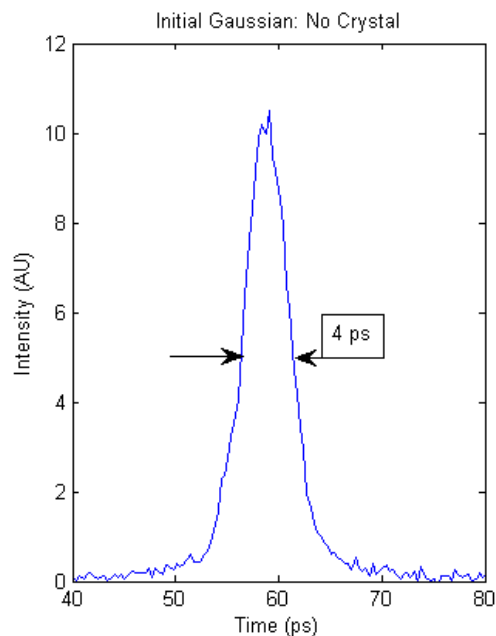


Figure 28. Initial laser pulse before any pulse forming

It was taken on the fastest sweep speed of the Synchroscan unit with < 1 nJ of energy / pulse. The measured pulse length was ~ 4 ps (FWHM).

2. First Crystal

The first crystal 35 mm long was then put in place and its angle adjusted until the two resulting sub-pulses were approximately equal. The effect of this crystal is seen in Figure 29, where the initial 35 mm crystal splits the initial pulse into two distinct and equal pulses with a gap of ~ 17 ps ± 1.3 ps.

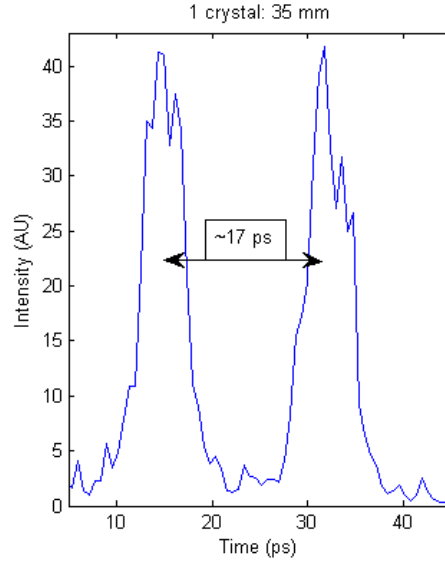


Figure 29. Individual sub-pulses after 35 mm crystal

This matches the calculated value of 16 ps separation to within 6% and falls within the standard deviation of the measurement. Due to the low group velocity dispersion, the two sub-pulses maintain the same length as the original pulse. During alignment, the output of the streak camera was viewed as a shot-to-shot profile with no averaging. The crystal was adjusted until a majority of the profiles showed sub-pulses of equal magnitude.

a. One Crystal Angle Study

To study the effect that the initial polarization would have on the first two sub-pulses, the angle of the 35 mm crystal was varied. The crystal was initially aligned to produce two equal sub-pulses, then its angle was altered by $\pm 5^\circ$ and $\pm 10^\circ$ to view the effect on the two resulting sub-pulses. The profiles were measured afterwards and compared with simulation results as seen in Figure 30.

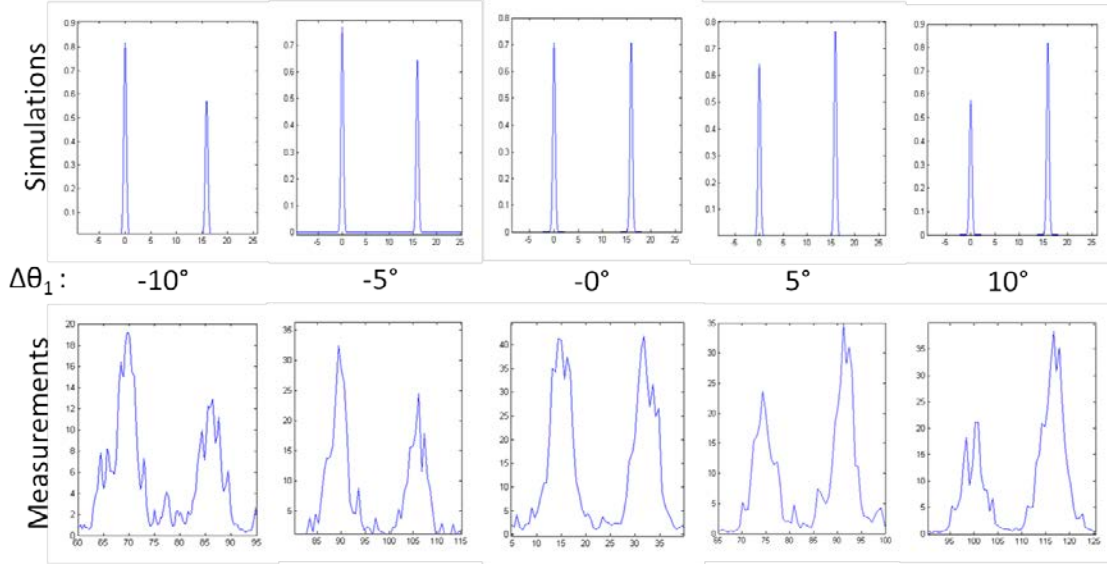


Figure 30. The effect of varying the alignment angle ($\Delta\theta_1$) of a single crystal. The extraordinary pulse is on the left and the ordinary pulse on the right in each profile. (Horizontal axes: Time (ps), Vertical Axes: Intensity (AU))

A nominal crystal orientation was found, presumably 0° , which split the initial pulse into two equal sub-pulses just as was done in the previous section. From this setting, the 35 mm crystal's orientation was adjusted to $\pm 5^\circ$ and $\pm 10^\circ$ in order to alter the angle between the OA of the crystal and the polarization of the laser pulses, $45^\circ - \Delta\theta_1$, causing the energy of the initial pulse to be transferred to the extraordinary and ordinary pulses by different percentages. In both simulations and experiments, the separation between the sub-pulses was ~ 17 ps and the general trend between the five different angles can be seen to follow the simulation's prediction. At 0° the center figure shows that the simulation and observed sub-pulses are equal in magnitude. At $\pm 5^\circ$, both the simulation and measurements show a difference in magnitude with the same orientation; -5° gives a larger percentage of energy to the extraordinary pulse, while $+5^\circ$ gives the ordinary wave more energy. At $\pm 10^\circ$, the orientation is again in agreement with a greater difference in the magnitudes.

3. Two Crystals

With the two longest crystals (35 mm and 17.5 mm) exactly aligned, the envelope should consist of four equidistant pulses with equal amplitudes. As was done with the

first crystal, the second crystal was adjusted until the majority of the four sub-pulses appeared to be of equal magnitude, as shown in Figure 31.

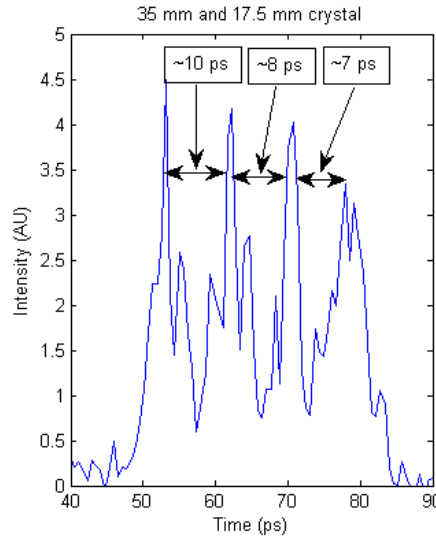


Figure 31. Pulse envelope after the 35 mm and 17.5 mm crystals

The four separated peaks are visible with the spacing between them approximately equal: ~ 10 ps, ~ 8 ps, and ~ 7 ps. These vary by $<12\%$ from the expected value of 8.0 ps for each separation. Again, the alignment was done viewing the shot-to-shot output of the streak camera and the crystal angle was adjusted accordingly. This supplied some error based on the shot-to-shot variation. The maximum difference in magnitude between any two pulses is $\sim 20\%$, and the pulses maintain the steep fall and rise time needed for the final pulse shape.

a. Two Crystal Angle Study

Just as was done with the single 35 mm crystal, the effect of an angle variation on the output profile with two crystals, 35 mm and 17.5 mm, was studied. The first crystal's optical axis was oriented to produce two equal sub-pulses before adjusting the second crystal to various angles, $\pm 5^\circ$ and $\pm 10^\circ$ from its nominal value. The results are shown in Figure 32.

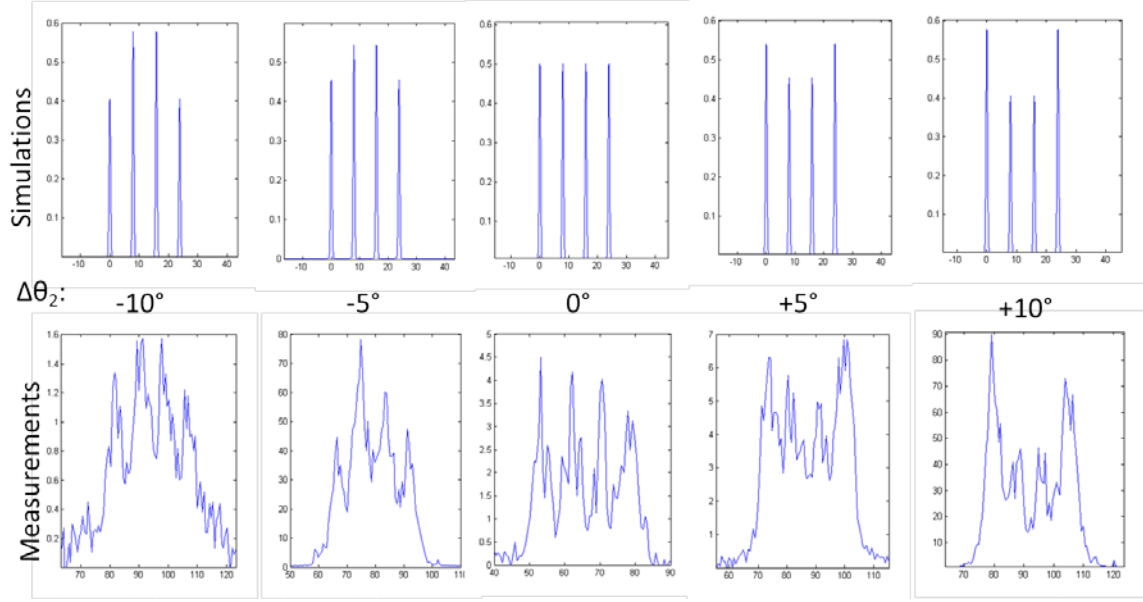


Figure 32. Two crystal study. The first crystal is optimally aligned ($\Delta\theta_1=0$), and the second crystal's alignment angle is varied from its nominal value ($\theta_2=45^\circ$) by $\Delta\theta_2 = \pm 5^\circ$ and $\pm 10^\circ$ (Horizontal axes Time (ps), Vertical Axes Intensity (AU))

Misaligning the second crystal to $\pm 5^\circ$ and $\pm 10^\circ$ shows the effect of the alignment angle on the final energy division into sub-pulses. With the optical axis of the two crystals correctly aligned, the initial pulse is divided into four approximately equal sub-pulses. As the second crystal is shifted slightly from the nominal angle, $\theta_2=45^\circ$, the distribution of energy from the initial two sub-pulses into the final four changes. How the energy is distributed into the final four sub-pulses is related to the orientation of the second crystal with respect to the polarizations of the sub pulses coming from the first crystal. As the two sub-pulses enter the second crystal, the effect that the misaligned second crystal has on each individual sub-pulse is different due to their orthogonal polarizations. This produces four final pulses of varying amplitude, but in a clear pattern. The code recreates these trends and allows the effect of the crystal misalignments to be predicted. The qualitative agreement between the simulated and observed patterns is excellent.

A second angle study with two crystals was performed much in the same manner as the previous one. The two crystals were initially aligned to the nominal 45° orientations, as was done in the previous study, to produce four approximately equal

pulses. However, in this example, the first crystal was now rotated in the $\pm 5^\circ$ and $\pm 10^\circ$. The results of this study are shown in Figure 33, where there is again excellent agreement between the patterns.

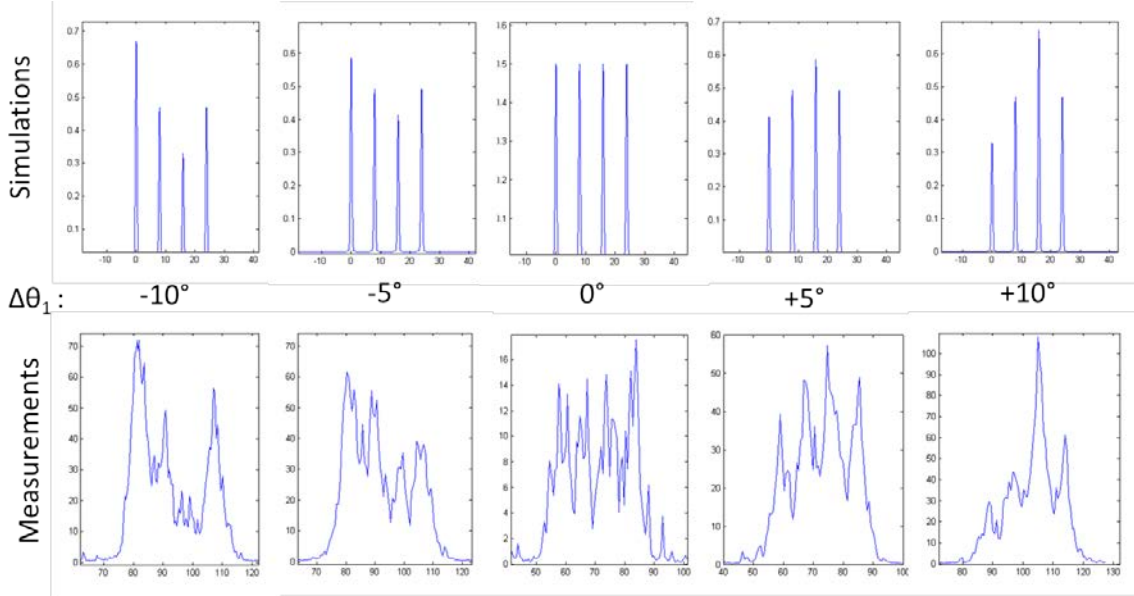


Figure 33. Two crystal study. Both crystals are initially optimally aligned ($\Delta\theta_1 = \Delta\theta_2 = 0$). The first crystal is then misaligned by $\Delta\theta_1 = \pm 5^\circ$ and $\pm 10^\circ$ (Horizontal axes Time (ps), Vertical Axes Intensity (AU))

In this study, the first crystal misalignment has two separate effects. The misalignment between the initial polarization and the crystal's orientation causes the initial pulse to be split into two unequal sub-pulses. The second effect is that these two unequal sub-pulses then have the wrong polarization with respect to the second crystal's OA. These two effects cause the overall envelope to vary as a factor of this initial angle with greater energy variation. The simulated and measured results still follow the same general pattern.

4. Three Crystals

The addition of the third crystal (8.75 mm) brings the total number of sub-pulses that create the envelope to eight. An example of this envelope is seen in Figure 34.

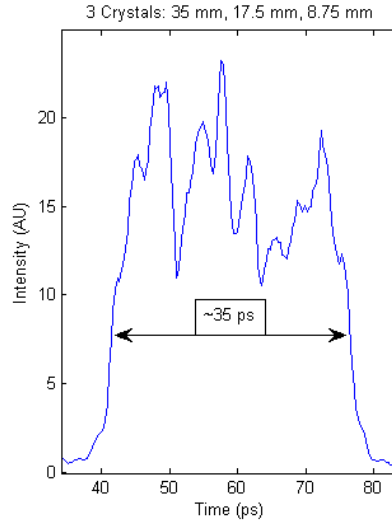


Figure 34. 35 mm, 17.5 mm and 8.75 mm crystal

There are no longer the four distinct peaks that were visible with the two crystal set. The length of this pulse is ~ 4 ps longer than is expected in the calculations, but this could be due to the resolution of the streak camera as well as noise in the streak camera.

5. Six Crystals

The last three crystals do not contribute much to the overall length of the pulse, but are used more to fill in the spaces between the pulses left by the previous crystals, in order to decrease the energy variation. Each crystal was added in place behind its predecessor, and then the output was optimized by viewing the real time shot-to-shot images. The four crystal and five crystal profiles are displayed in Figure 35.

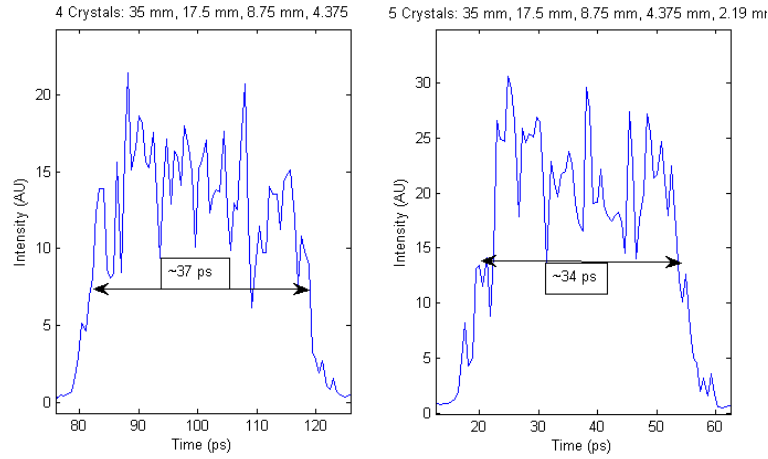


Figure 35. Four crystal (left) and five crystal (left) profiles

The shot-to-shot noise diminishes the discernible difference between the two profiles. Finally, the last crystal was put in place and the pulse profile was measured several times. These are displayed in Figure 36.

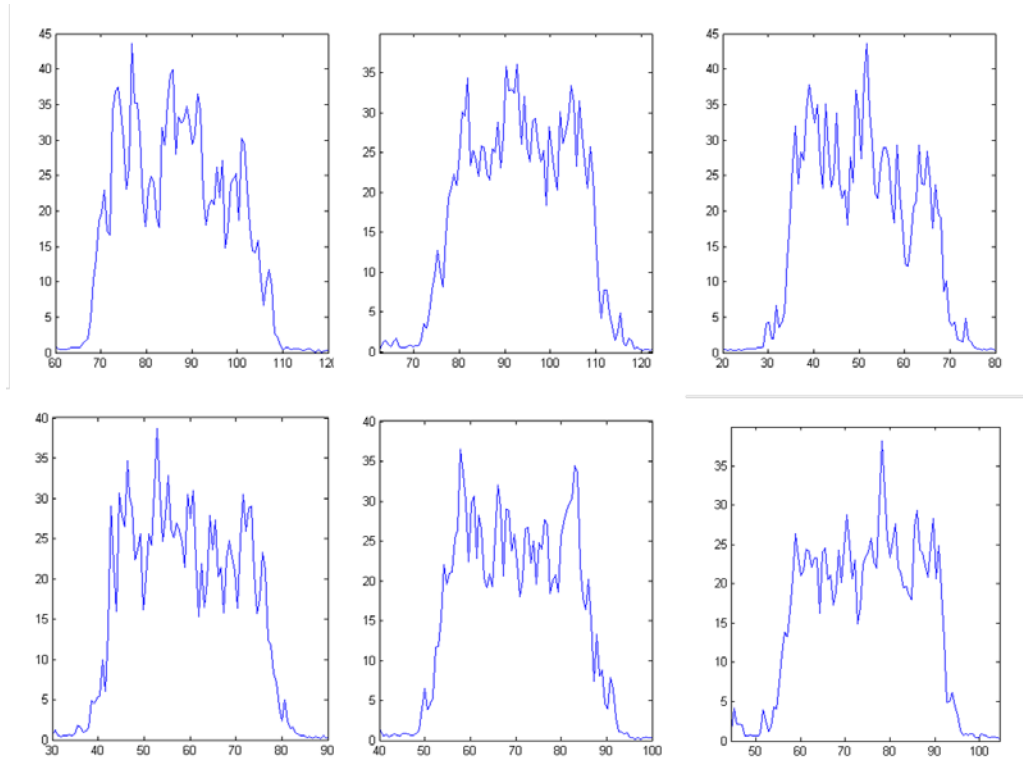


Figure 36. Profiles of final pulse shape after six crystal stack (Horizontal axes Time (ps), Vertical Axes Intensity (AU))

The six crystals worked to create a final pulse with a length that reproducibly measured $\sim 35 \text{ ps} \pm 0.5 \text{ ps}$. This is very close to the calculated 32 ps that was expected, and fits within the resolution of the streak camera. The average energy variation was seen to be $\sim 40\%$. These large energy variations changed on a shot-to-shot basis. As the six crystals were added, the single pulse evolved into the predicted $\sim 35 \text{ ps}$ long pulse with a sharp rise and fall time of $\sim 4 \text{ ps}$. The longitudinal energy variations seemed random and could be due to noise in the streak camera.

F. POSSIBLE SOURCES OF ERROR

1. Systematic Errors

Misalignments in the crystals will lead to different structures along the profile of the laser pulse. These overlying trends are visible in Figure 30, but are generally overwhelmed by the shot-to-shot fluctuation of the data. To properly dilute the random pulse variations, several pulse profiles can be averaged together in order to observe the steady trends caused by the misalignments in the crystal. Three separate averages of 10 pulses were taken and are shown in Figure 37.

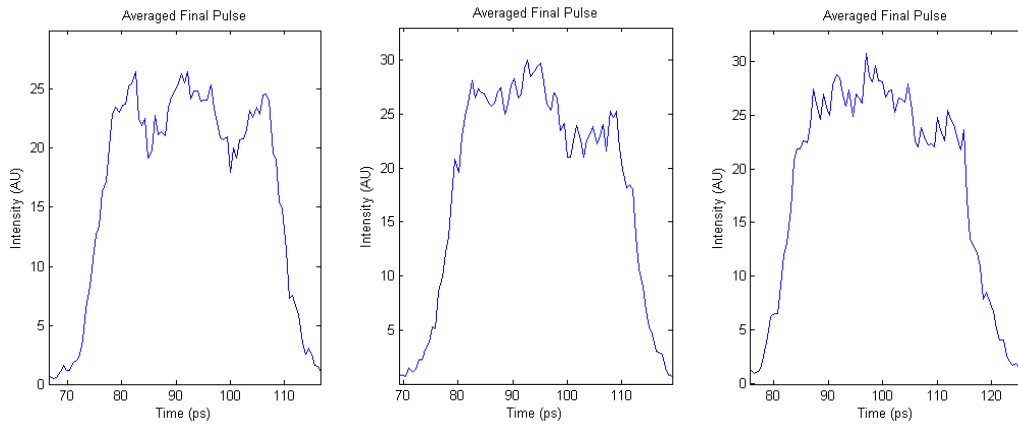


Figure 37. Three final profiles, each an average of 10 single shot pulse profiles

There is a systematic problem that may be due to misalignments in the crystals, which produce energy variations along the pulse profile. These types of variations can be reproduced using the simulation code, as are shown in Figure 38.

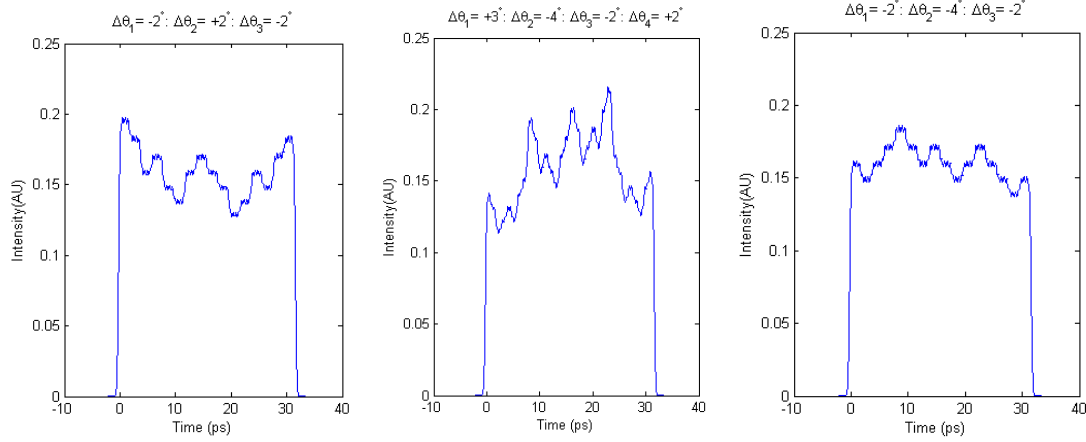


Figure 38. Three simulations with crystal misalignments. Left: $\Delta\theta_1 = -2^\circ$, $\Delta\theta_2 = +2^\circ$, $\Delta\theta_3 = -2^\circ$. Center: $\Delta\theta_1 = +3^\circ$, $\Delta\theta_2 = -4^\circ$, $\Delta\theta_3 = -2^\circ$, $\Delta\theta_4 = +2^\circ$. Right: $\Delta\theta_1 = -2^\circ$, $\Delta\theta_2 = -4^\circ$, $\Delta\theta_3 = -2^\circ$.

In the labeling of the plots in Figure 38, $\Delta\theta_1$, $\Delta\theta_2$, $\Delta\theta_3$, $\Delta\theta_4$ are the misalignments from the nominal values for crystals one, two, three, and four, respectively. These examples demonstrate the types of profiles that can be created by simple crystal misalignments. The first crystals have more of an impact on the profile's energy variation though even misalignment in the last one can lead to significant energy variations. With an averaged output from the streak camera the crystals could be adjusted accordingly to produce a flatter profile.

2. Random Errors

The shot-to-shot fluctuation between pulses that occurred during data acquisition was persistent through each measurement. This variation could come from the drive laser or intrinsic noise from the streak camera. Also, imperfections in the micro-channel plate could cause different areas to be amplified to different amounts, inducing an energy variation. In terms of variations in the laser, it could be a polarization jitter, where the polarization from shot-to-shot would vary slightly before propagating through the crystal stack. If the initial polarization is not aligned properly with the first crystal, the initial two sub-pulses will not be of equal amplitude, and this error will be compounded as it propagates through the crystal stack, creating an energy variation.

VIII. CONCLUSION

A laser pulse shaping technique was studied, assembled and measured in the thesis. While the initial goal of shaping and measuring the final profile of a UV laser pulse was not possible, the pulse stacker worked to shape a green pulse and the results agreed well with theoretical calculations and simulations. The measured overall pulse length of ~ 35 ps closely matched theoretical predictions of ~ 32 ps. From this we can infer that the pulse stacker would create a UV laser pulse of ~ 56 ps, as predicted by the simulations. The overall pulse profile was measured and controlled using the birefringent crystal stacker in an understood way. Enhancements to the stability of the drive laser or a reduction of noise in the streak camera could lead to a better understanding of the entire system and result in a more homogeneous longitudinal profile.

THIS PAGE INTENTIONALLY LEFT BLANK

LIST OF REFERENCES

- [1] Elder, F. R.; A. M.; Langmuir, R. V.; Pollock, H. C., "Radiation from Electrons in a Synchrotron" (1947) *Physical Review*, vol. 71, Issue 11, pp. 829-830.
- [2] "Conceptual Design Report for the Upgrading of Sesame to 2GeV," White Paper, Sesame, Jul. 2002.
- [3] F. Sannibale, "Electron Sources and Injectors, Lecture 2", Joint US-CERN-Japan-Russian School on Particle Accelerators, Erice, IT, April 2011.
- [4] H. Winick, S. Doniach, *Synchrotron Radiation Research*. New York: Plenum, 1980.
- [5] H. Winick, "Fourth Generation Light Sources," Proc. Particle Accelerator Conference (PAC97), 1997.
- [6] D. Halliday and R. Resnick, *Fundamentals of Physics*, New York, NY: Wiley, 2008.
- [7] M.M. Woolfson, *An Introduction to X-ray Crystallography*. Cambridge: Cambridge UP, 1970.
- [8] G. Bunker, *Introduction to XAFS: A Practical Guide to X-ray Absorption Fine Structure Spectroscopy*, Cambridge: Cambridge UP, 2010.
- [9] L. Elias, W. Fairbank, J. Madey, "Observation of Stimulated Emission of Radiation by Relativistic Electrons in a Spatially Periodic Transverse Magnetic Field," *Physical Review Letters*, Vol. 36, no. 13, pp. 717-720, 1976.
- [10] J. Teichert, "ELBE Superconducting RF photoinjector (SRF Gun)," [Online]. Available: <http://www.hzdr.de/db/Cms?pNid=234>. [Accessed: Feb. 2012].
- [11] F. Sannibale, D. Filippetto, C. Papadopoulos, "Schemes and Challenges for Electron Injectors Operating in High Repetition Rate X-ray FELs," *Journal of Modern Optics*, Vol. 58, no. 16, pp. 1419-1437, Sep. 2011.
- [12] J. Graber, "Superconducting RF Cavities: A Primer," [Online]. Available: <http://www.lepp.cornell.edu/Research/AP/SRF/SrfCavitiesAPrimerOne.html>. [Accessed: Feb. 2012].
- [13] Centre Laser Infrarouge d'Orsay, "What is a Free-Electron laser?," [Online]. Available: http://clio.lcp.u-psud.fr/clio_eng/FELrad.html. [Accessed: Feb. 2012].

- [14] P. Pernet, “A Proof-of-Principle Echo-Enabled Harmonic Generation Free Electron Laser Experiment at SLAC,” Master’s thesis, École Polytechnique Fédérale de Lausanne, 2010.
- [15] W.B. Colson, “Free Electron Lasers,” Class notes for PH4055, Department of Physics, Naval Postgraduate School, Monterey, CA, SEMESTER 2010.
- [16] “Separatrix for a Simple Pendulum,” [Online]. Available: http://en.wikipedia.org/wiki/File:Separatrix_for_a_Simple_Pendulum.png. [Accessed: Mar. 2012].
- [17] G. Dattoli, A. Renieri, A. Torre, *Lectures on the Free Electron Laser Theory and Related Topics*, World Scientific, 1993.
- [18] C.A. Brau, *Free Electron Lasers*. Boston: Academic Press, 1990.
- [19] W.B. Colson, J. Blau, J.W. Lewellen, “Free Electron Lasers in 2008.” *Proc. Int’l Free Electron Laser Conference (FEL08)*, 2008.
- [20] R. Alley, V. Bharadwaj, J. Clendenin, “The Design for the LCLS RF Photoinjector,” *Proc. Int’l Free Electron Laser Conference (FEL 98)*, 1998.
- [21] Arenholz, Elke, “Toward Control of Matter: Basic Energy Science Needs for a New Class of X-Ray Light Sources,” [Online]. Available: <http://www.escholarship.org/uc/item/9n97q0g0>. [Accessed: Feb 2012].
- [22] B. Schoenlein, “The Next Generation Light Source: Facility Overview and Applications for Understanding Correlated Materials,” [Online]. Available: www.lbl.gov/kaindl/Novel_Trends_in.../Schoenlein_ALS_2011.pdf. [Accessed: May 2012].
- [23] F. Sannibale, “Design Studies for a Next Generation Light Source Facility”, Naval Postgraduate School Colloquium, Monterey, CA, Jun. 2011.
- [24] F. Sannibale, “APEX Project Phases 0 and I Status and Plans and Activities for Phase II,” *Free Electron Laser Conference (FEL11)*, 2011.
- [25] F. Sannibale, “Electron Sources and Injectors, Lecture 1”, Joint US-CERN-Japan-Russian School on Particle Accelerators, Erice, IT, April 2011.
- [26] K. J. Middleman, “Photocathode Preparation System for the ALICE Photoinjector,” *Proc. AIP Conference*, Charlottesville, VA, 2008, pp. 1089-1093.

- [27] K. Baptiste. (2009), “A CW normal-conductive RF gun for free electron laser and energy recovery linac applications,” [Online]. Available: <http://escholarship.org/uc/item/1qz6w4k1>. [Accessed: Feb. 2012].
- [28] S. Lederer, G. Asova, J.W. Baehr, *et al*, “Investigation on the Thermal Emittance of Cs₂Te Photocathodes at PITZ,” Proc. FEL 2007 (FEL07), 2007.
- [29] F. Sannibale, “Schemes and challenges for electron injectors operating in high repetition rate X-ray FELs,” *Journal of Modern Optics*, Vol. 58, No. 16, pp. 1419-1437, Sep, 2011.
- [30] H. Tomizawa, “Advanced Laser Pulse Shaping,” Joint ICFA Advance Accelerator and Beam Dynamics Workshop, Maui, HI, 2009.
- [31] O. J. Luiten, “How to Realize Uniform Three-Dimensional Ellipsoidal Electron Bunches,” Phys. Rev. Lett, Vol. 93, No. 9, Aug, 2004.
- [32] W.B. Colson, “Electric Ship Weapon Systems,” Class notes for PH4858, Department of Physics, Naval Postgraduate School, Monterey, CA, SEMESTER 2010.
- [33] “Elliptically and Circularly Polarized Light Waves,” [Online]. Available: <http://www.microscopyu.com/tutorials/java/polarized/waveform3d/index.html>. [Accessed: Mar. 2012].
- [34] “Wave Packet,” [Online]. Feb. 2012, Available: <http://www.physics.uiowa.edu/~umallik/adventure/quantumwave.html>. [Accessed: Mar. 2012].
- [35] “Refractive Index Fused Silica,” [Online]. Available: http://refractiveindex.info/?group=GLASSES&material=F_SILICA. [Accessed: Mar. 2012].
- [36] RP Photonics, “Encyclopedia of Laser Physics and Technology: Sellmeier Formula,” [Online]. Available: Feb. 2012, http://www.rp-photonics.com/sellmeier_formula.htm. [Accessed: Mar. 2012].
- [37] F. L. Pedrotti and L. S. Pedrotti, *Introduction to Optics*, 2nd ed. Upper Saddle River, NJ: Prentice-Hall, 1993.
- [38] D.B. Murphy, K. R. Spring, *et al*, “Introduction to Optical Birefringence,” [Online]. Available: <http://www.microscopyu.com/articles/polarized/birefringenceintro.html>. [Accessed: Mar. 2012].

- [39] “Refractive Index ellipsoid of uniaxial crystal.” [Online]. Feb. 2012, Available: <http://www.fiberoptics4sale.com/wordpress/what-is-optical-circulator-and-its-applications/>. [Accessed: Mar. 2012].
- [40] E. Treacy, “Optical Pulse Compression with Diffraction Gratings”, *Journal of Quantum Electronics*, vol. 5, issue 9, pp. 454-458.
- [41] J. Feng, “Drive Laser System for the Advanced Photon-Injector Experiment at the LBNL,” *Particle Accelerator Conference*, New York, NY, 2011.
- [42] M.M. Fejer, G.A. Magel, D.H. Jundt, *et al*, “Quasi-phase-matched second harmonic generation: tuning and tolerances,” *IEEE Journal of Quantum Electronics*, vol.28, no.11, pp.2631-2654, Nov 1992, doi: 10.1109/3.161322.
- [43] Christos Papadopoulos (PhD), [Private Conversation], Jan. 2012.
- [44] D. H. Dowell, “LCLS Drive Laser Shaping Experiments,” *Free Electron Laser Conference*, Liverpool, UK, 2009.
- [45] S. Zhou, D. Ouzounov, *et al*, “Efficient Temporal Shaping of Ultrashort Pulses with Birefringent Crystals,” *Conference on Lasers and Electro-Optics*, Baltimore, MD, 2007.
- [46] “Retardation Plate Theory,” White Paper, Special Optics.
- [47] I. Bazarov, D. Ouzounov, *et al*, “Efficient Temporal Shaping of Electron Distribution for High-brightness Photoemission Electron Guns,” *Phys. Rev. ST Accel. Beams*, Vol. 11, Issue 4, 2008. doi: 10.1103/PhysRevSTAB.11.040702.
- [48] “Alpha BBO,” [Online]. Available: <http://www.agoptics.com/Birefringent-Crystal/alpha-BBO.htm>. [Accessed: Mar. 2012].
- [49] “The Effect of Dispersion on Ultrashort Pulses,” White Paper, Newport Corporation.
- [50] “Polarization Optics Tutorial: Polarizers, Waveplates, Rotators, and Lyot Filters,” White Paper, Ray Williamson Consulting, 2005.
- [51] “Instruction Manual for Universal Streak Camera C5680 Series,” Technical note, Hamamatsu Photonics.

INITIAL DISTRIBUTION LIST

1. Defense Technical Information Center
Ft. Belvoir, Virginia
2. Dudley Knox Library
Naval Postgraduate School
Monterey, California
3. Professor William B. Colson
Naval Postgraduate School
Monterey, CA
4. Professor Keith Cohn
Naval Postgraduate School
Monterey, CA
5. Dr. Fernando Sannibale
Lawrence Berkeley National Laboratory
Berkeley, CA
6. Dr. Daniele Filippetto
Lawrence Berkeley National Laboratory
Berkeley, CA
7. Mr. Edward Pogue
Boeing Corporation
Santa Fe, NM